

# Solid-body trajectoids shaped to roll along desired pathways

<https://doi.org/10.1038/s41586-023-06306-y>

Received: 2 January 2022

Accepted: 9 June 2023

Published online: 9 August 2023

 Check for updates

Yaroslav I. Sobolev<sup>1,5</sup>, Ruoyu Dong<sup>1,5</sup>, Tsvi Tlusty<sup>1,2</sup>, Jean-Pierre Eckmann<sup>3</sup>, Steve Granick<sup>1,4</sup> & Bartosz A. Grzybowski<sup>1,4</sup>

In everyday life, rolling motion is typically associated with cylindrical (for example, car wheels) or spherical (for example, billiard balls) bodies tracing linear paths. However, mathematicians have, for decades, been interested in more exotically shaped solids such as the famous ovoids<sup>1</sup>, sphericons<sup>2</sup>, polycons<sup>3</sup>, platonicons<sup>4</sup> and two-circle rollers<sup>5</sup> that roll downhill in curvilinear paths (in contrast to cylinders or spheres) yet indefinitely (in contrast to cones, Supplementary Video 1). The trajectories traced by such bodies have been studied in detail<sup>6–9</sup>, and can be useful in the context of efficient mixing<sup>10,11</sup> and robotics, for example, in magnetically actuated, millimetre-sized sphericon-shaped robots<sup>12,13</sup>, or larger sphericon- and oloid-shaped robots translocating by shifting their centre of mass<sup>14,15</sup>. However, the rolling paths of these shapes are all sinusoid-like and their diversity ends there. Accordingly, we were intrigued whether a more general problem is solvable: given an infinite periodic trajectory, find the shape that would trace this trajectory when rolling down a slope. Here, we develop an algorithm to design such bodies—which we call ‘trajectoids’—and then validate these designs experimentally by three-dimensionally printing the computed shapes and tracking their rolling paths, including those that close onto themselves such that the body’s centre of mass moves intermittently uphill (Supplementary Video 2). Our study is motivated largely by fundamental curiosity, but the existence of trajectoids for most paths has unexpected implications for quantum and classical optics, as the dynamics of qubits, spins and light polarization can be exactly mapped to trajectoids and their paths<sup>16</sup>.

Let us begin by drawing some curve  $T$  on a plane, copying it multiple times to form an infinite periodic trajectory  $T_{\infty}$ , and inclining the plane slightly (Fig. 1a). The question we then ask is whether it is possible to design a solid body—which we will call a ‘trajectoid’—to roll exactly along  $T_{\infty}$  without slipping or pivoting (in which ‘pivoting’ means spinning about a normal to the plane at a point of contact).

To develop intuition about engineering such objects, we begin with the simplest case: a cylinder of radius  $r$  rolling without slipping or pivoting over a horizontal plane is a trajectoid of a straight line (Fig. 1b). For the preferred, linear path, the cylinder’s centre of mass (CM) is always at a height  $r$  above the plane (Fig. 1b, green dot): in this sense, the path is an ‘equipotential’ one, and any deviation from it would raise the cylinder’s CM (to the red dot), thereby increasing the gravitational potential energy (green surface).

Extending to a flat path  $T$  composed of several straight lines (Fig. 1c), we consider a ‘virtual’ assembly of a heavy sphere (radius  $r$ ) encased inside a weightless spherical ‘ghost’ shell of radius  $R > r$ . We shave off part of the shell to leave behind a locally cylindrical region of radius  $r$ : in this way, the object can roll along the first segment, with the points of attachment of the inner, heavy sphere tracing precisely this portion

of the path  $T$ . When the starting point of the next segment is reached, we trim the shell to define another local cylinder to roll along this new direction. The procedure is then repeated until reaching the end of the polygonal path (or, in general, of a curvilinear path approximated by a union of infinitesimally short linear segments). The body thus shaped can be construed as a piecewise combination of gradually reorienting cylinders whose axes remain parallel to the plane below, and pass through the body’s CM. This CM always remains at a height  $r$  above the plane, and the planar path defines an equipotential ‘trench’ in the trajectoid’s landscape of gravitational energy (Fig. 1b). Whereas the sphere touches the plane at a single point at a time, the final shape touches it at many points at once (as with cylinder-to-plane contact), giving stability to the roll. Some examples illustrating the morphing procedure for different trajectories and for different values of  $R/r$  are shown in Fig. 1d,e.

## Condition for trajectoid existence

For an object to qualify as a trajectoid, it must periodically regain its initial three-dimensional orientation. Noting that the points of the object’s contact with the planar trajectory  $T$  also trace a certain curve

<sup>1</sup>Center for Soft and Living Matter, Institute for Basic Science (IBS), Ulsan, South Korea. <sup>2</sup>Department of Physics, Ulsan National Institute of Science and Technology (UNIST), Ulsan, South Korea.

<sup>3</sup>Department of Theoretical Physics and Mathematics Section, University of Geneva, Geneva, Switzerland. <sup>4</sup>Department of Chemistry, Ulsan National Institute of Science and Technology (UNIST), Ulsan, South Korea. <sup>5</sup>These authors contributed equally: Yaroslav I. Sobolev, Ruoyu Dong. ✉e-mail: yaroslav.sobolev@gmail.com; tsvitlusty@gmail.com; Jean-Pierre.Eckmann@unige.ch; sgranick@gmail.com; nanogrzzybowski@gmail.com

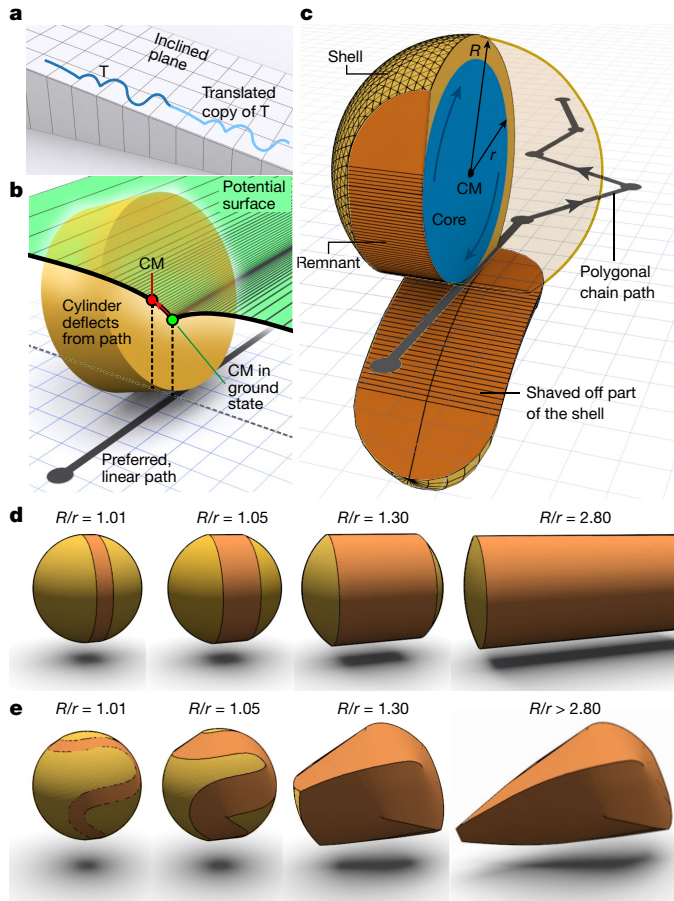


**Fig. 1 | Rolling paths and trajectoid shapes.** **a**, An arbitrary curve  $T$  (dark blue) drawn on an inclined plane (grid) serves as one period of an infinite translationally symmetric trajectory  $T_\infty$  to be traced by the trajectoid. **b**, A cylinder (gold) rolling along the plane (blue grid) must tilt sideways, as shown, to deviate from its preferred linear path of rolling (thick grey line on the grid). Such a tilt inevitably raises the cylinder's CM (red dot) along a cycloid-like curve (solid black) away from CM's original level (green dot): the preferred linear path corresponds to a trench in the gravitational potential landscape (green surface, also see Extended Data Fig. 6). For an illustration in frontal projection, see Extended Data Fig. 1a. **c**, The design of a trajectoid shape starts with a rigid core (blue) of radius  $r$  surrounded by a massless concentric shell (gold colour) of radius  $R > r$ . This composite structure, shown here in central cross-section, is forcibly moved in infinitely small steps such that the spherical core rolls along the target path (grey polygonal chain) without slipping or pivoting (Supplementary Video 1). To allow such rolling, the shell is 'shaved' to leave a patch of cylindrical surface (orange). The point CM is the centre of mass of the core, and therefore of the whole assembly. **d**, Trajectoids for a linear path using different ratios  $R/r$  consist of a cylindrical part (orange) of radius  $r$  and two surviving spherical segments of the shell (gold). **e**, Trajectoids for the curvilinear path (same as in Fig. 2a and experimentally realized in Fig. 4d) using different ratios  $R/r$ . At  $R/r = 1.01$ , the body is still roughly spherical but for higher values shown, the shape becomes complex (and does not change for  $R/r \geq 2.80$ ) and has improved stability due to deeper potential energy trench (b and Extended Data Fig. 1a).

on the surface of this object's inner, heavy sphere (Figs. 1c and 2a), the condition for periodic motion can be recast in terms of the rotation group acting on this rolling sphere. Specifically, an  $n$ -period trajectoid exists for a translationally invariant path  $T_\infty$  if there exists a ball of finite radius  $r$ , which, after rolling (without slipping or pivoting) along  $n$  periods  $T$  composing the subpath  $T_n = A\Omega$ , regains the same orientation at endpoint  $\Omega$  as it initially had at starting point  $A$ . Repeating this cycle, the trajectoid then rolls indefinitely along  $T_\infty$ .

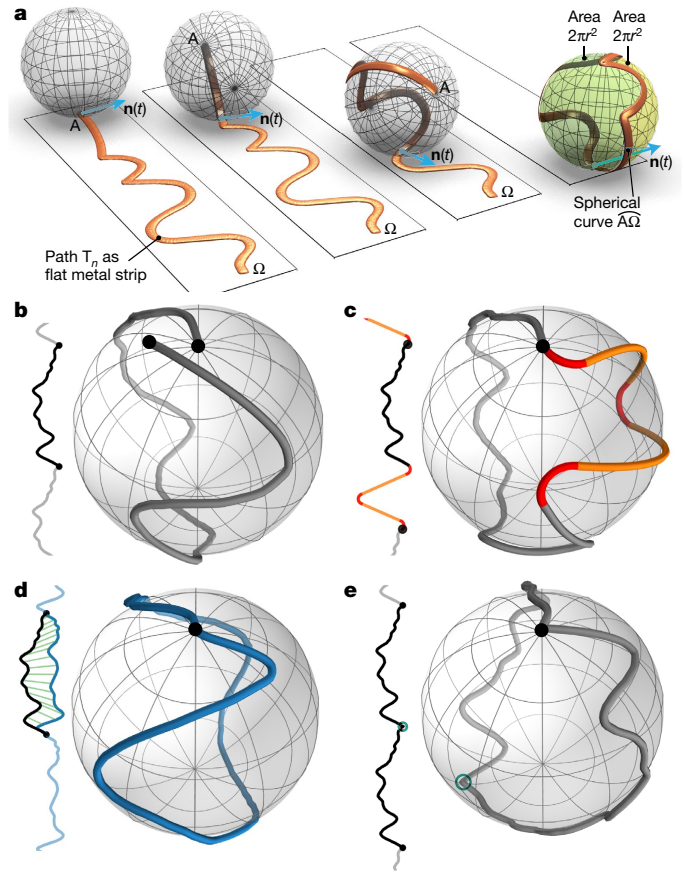


**Fig. 2 | Path-to-sphere mapping and trajectoid existence.** **a**, Condition necessary for trajectoid existence. A flat path  $T_n = A\Omega$  (starting at point  $A$  and ending at point  $\Omega$ ) can be construed as a sticky metal strip that easily bends out of the plane yet maintains its length and geodesic (initially, in-plane) curvature. This metal strip attaches (maps) to the sphere being rolled along it and becomes the sequence of the sphere-plane contact points. For a trajectoid of  $A\Omega$  to exist, on reaching the point  $\Omega$ , the sphere must arrive at the same 3D orientation as it had at the starting point  $A$ . This condition is equivalent to  $\widehat{A\Omega}$  being a closed spherical curve splitting the sphere's surface into two equal areas  $2\pi r^2$  (shaded green and yellow on the rightmost sphere in **a**). **b–d**, When a path  $T$  (**b**, one period) does not map onto a closed curve on a sphere it can be either appended with a bridge (**c**, coloured in red and orange here) or deformed (**d**, green lines connect the points of original black  $T$  to respective points of its deformed blue version, see main text and Methods for details). Some  $T$  can be transformed in this way to yield viable one-period trajectoids (experiments in Fig. 4d, e, g, n, o). **e**, By contrast, a two-period trajectoid exists for most paths and no amendments to the path are needed (the green circle shows where the two periods meet).

The path  $T_n = A\Omega$  can be represented by the dependence of its normal  $\mathbf{n}(t) = (\cos\psi(t), \sin\psi(t), 0)$  (blue in Fig. 2a) on the arc length  $t$  along the trajectory, where  $\psi$  is the angle  $\mathbf{n}(t)$  forms with the planar projection of gravity. Alternatively,  $T_n$  can be specified by the curvature  $\kappa(t) = d\psi/dt$  and the initial angle  $\psi(0)$  (ref. 17). The translational periodicity of the path  $T_n$  (as in Fig. 1a) indicates that the curvature obeys an index theorem<sup>18</sup>,

$$\psi(t) \Big|_T = \int_T \kappa(t) dt = 2\pi I_T, \quad (1)$$

where  $I_T$  is the rotation index of the period  $T$ , for example,  $I_T = 0$  if  $T$  does not self-intersect. A complementary scenario was recently considered<sup>19</sup> where bodies are designed such that their rolling paths are confined to a finite region on the plane. These 'non-trajectoids'

# Article

therefore violate the property in equation (1) and are bound to halt when rolling autonomously down a slope.

Let us now model the rolling motion in a frame of reference in which the sphere's centre is stationary and the sphere rotates around it. We approximate the planar path  $A\Omega = \mathbf{n}(t)$  by a polygon made of  $N$  short straight segments of length  $\delta t$ . In the said coordinate system, each segment  $\delta t$  with starting point  $t_i$  induces a rotation of the sphere around an axis parallel to the normal to the path  $\mathbf{n}(t_i)$  (blue arrows in Fig. 2a) by an angle  $\delta t/r$  (Methods). The rotation is captured by a rotation matrix  $R_i = \exp[(\delta t/r)(\mathbf{n}(t_i) \cdot \mathbf{L})]$ , where the generators of the rotation group  $SO(3)$  are  $\mathbf{L} = (L_x, L_y, L_z)$ . As the sphere is rolling, the rotations  $R_i$  act on the sphere sequentially, progressing from the first to the last segment (Fig. 1c), and the overall rotation  $R_{A\Omega}$  is then their 'time-ordered product',  $R_{A\Omega} = R_N \cdots R_2 R_1$ . In the limit  $N \rightarrow \infty$ , the overall rotation  $R_{A\Omega}$  becomes an infinite product of minute rotations, which takes the form of a time-ordered exponential, familiar from quantum field theory<sup>20</sup>,

$$R_{A\Omega} = \mathcal{T} \left[ \exp \left( \frac{1}{r} \int_A^\Omega dt \mathbf{n}(t) \cdot \mathbf{L} \right) \right] \quad (2)$$

where the time-ordering operator  $\mathcal{T}$  ensures that the rotations and the generators are multiplied in the correct order according to their position  $t$  along the path. In terms of rotation matrices, the trajectoid must obey  $R_{A\Omega} = 1$ , where  $1$  is the identity matrix.

Per the illustration in Fig. 2a, this condition can be visualized by imagining that the flat curve  $T_n = A\Omega$  is cut out of a flexible metal sheet as a narrow ribbon that can bend out of plane and stick onto the rolling ball, producing a curve  $\widehat{A\Omega}$  on the sphere. As the sticking ribbon deforms only out-of-plane, it conserves the arc length  $t$  (by forbidding stretching due to slipping) and the geodesic curvature  $\kappa(t)$  (by forbidding in-plane bending due to pivoting). Thus,  $\kappa(t)$  would now become the geodesic curvature of the 'attached' spherical curve  $\widehat{A\Omega}$ .

The  $R_{A\Omega} = 1$  condition implies that  $\widehat{A\Omega}$  is a closed curve on the sphere. By the Gauss–Bonnet theorem<sup>18,19,21</sup>,  $\widehat{A\Omega}$  encircles an area,  $S = 2\pi r^2(1 - I_{\widehat{A\Omega}})$ , where the rotation index is  $I_{\widehat{A\Omega}} = (2\pi)^{-1} \oint dt \kappa(t)$ . The invariance of  $\kappa(t)$ , as illustrated by the sticky ribbon, indicates that its integral, the rotation index, is also conserved,  $I_{\widehat{A\Omega}} = I_{A\Omega} = nI_T$ . Hence, by equation (1), the area enclosed by  $\widehat{A\Omega}$ , on either side (green and yellow in the rightmost panel of Fig. 2a) is  $S = 2\pi r^2(1 - I_{A\Omega}) = 2\pi r^2$ , for  $I_T = 0$ . If  $\widehat{A\Omega}$  self-intersects, then the standard definitions of signed oriented area are in effect<sup>18</sup> and, with this convention, the area must be a multiple of  $2\pi r^2$ .

## One- and multiple-period trajectoids

It is obviously not guaranteed that an arbitrary one-period path  $T$  will map onto the rolling sphere as a closed loop, let alone enclose an area of exactly  $2\pi r^2$ . In fact, these conditions are typically not met and one-period trajectoids ( $n = 1$ ) are expected to be rare. This said, a given path  $T$  can sometimes be heuristically adjusted to produce a similar trajectory that does close up on a sphere and encloses  $2\pi r^2$  areas. One way to do so is by appending a specially constructed bridge to the given path (Fig. 2b,c, see details in Extended Data Fig. 3 and Methods). Another is to deform the given path as illustrated in Fig. 2d and Extended Data Fig. 2. In both approaches, the quantity to minimize is the angle  $\theta$  of mismatch between the initial and final orientations of the sphere on completing one path period  $T$  (for details, see Methods). As we will see later, these procedures generally produce trajectoids that, when physically fabricated, trace the adjusted paths faithfully and periodically (Fig. 4).

In striking contrast to  $n = 1$ , we prove below that two- and higher-period trajectoids,  $n \geq 2$ , exist for a broad class of paths defined by a general property  $\pi$  described below. In our numerical experiments, a random graph drawn on the plane always belonged to this class. This includes wild self-intersecting and convoluted graphs (Extended Data Fig. 4).

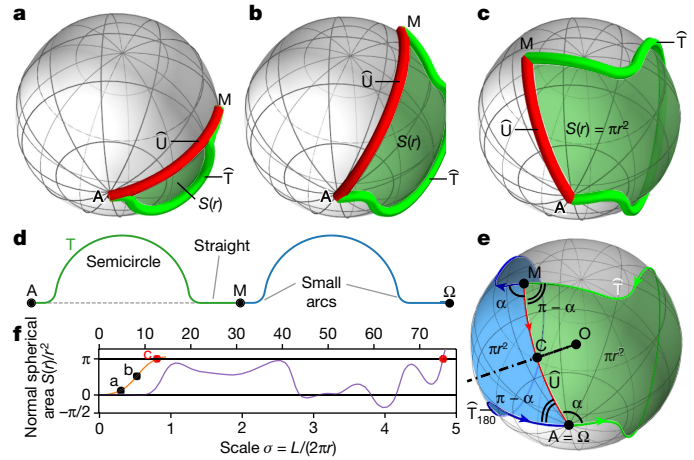


**Fig. 3 | Property  $\pi$  and TPT theorem.** Illustration of property  $\pi$  ensuring the existence of TPTs (see text for details) for a path whose period (green or blue in **d**) consists of a semicircle, two straight lines and two small arcs to smooth the corners. **a–c**, Spherical trace  $\widehat{T}$  (green) of the contact point on rolling a unit sphere along one period of the path. We use control parameter  $\sigma = L/(2\pi r)$ —the ratio of the path's length  $L$  and the sphere's circumference (for example,  $\sigma = 1$  for a great circle). **a**,  $\sigma = 0.304$ . **b**,  $\sigma = 0.526$ . **c**,  $\sigma = 0.81$ . As  $\sigma$  increases from **a** to **c**, the area  $S(\sigma)$  (shaded green) enclosed by the green spherical trace  $\widehat{T}$  and the red arc  $\widehat{U}$  also increases (plotted in **f**, orange curve and bottom axis) and eventually reaches  $\pi$  in **d** (also shown by a left red dot in **f**). For an animation, see Supplementary Video 3. Points marked on the orange curve  $S(\sigma)$  in **f** correspond to **a–c**. The purple curve in **f** is a respective plot for a random walk path (Extended Data Fig. 4g), its trajectoid solution marked by the rightmost red circle. Note that this function is non-monotonic (text). **e**, Illustration of the proof of the TPT theorem. See text and Supplementary Video 3 for details.

## Two-period trajectoid theorem

Two-period trajectoids (TPTs) can be constructed for paths  $T_\infty$  whose period  $T$  has the following property  $\pi$ : As a sphere of finite radius  $r > 0$  rolls along the period  $T = AM$ , the contact point traces on the sphere's surface a spherical curve  $\widehat{T}$ , which is not necessarily closed (green in Fig. 3a–c). Together,  $\widehat{T}$  and a great arc  $\widehat{U}$  (red) connecting its ends  $M$  and  $A$  enclose some oriented spherical area  $S(r)$ . The condition requires that there exists an  $r$  for which  $S(r)/r^2 = \pm\pi$  (red dots in Fig. 3f).

The proof relies on the following simple observation: by the Gauss–Bonnet theorem, the integral of geodesic curvature along a spherical curve with property  $\pi$  is, modulo  $2\pi$ ,  $\oint dt \kappa(t) = 2\pi - S(r)/r^2 = \pi$  (details in Methods). However, the curvature integral vanishes along  $\widehat{T}$  (by periodicity, equation (1)), and along the great arc  $\widehat{U}$  (because it is geodesic), so the only remaining contribution comes from the corners  $A$  and  $M$  whose angles therefore add up to  $\pi$  ( $\pi - \alpha$  and  $\alpha$  in Fig. 3e). This property allows us to draw a  $180^\circ$ -rotated image  $\widehat{T}_{180}$  (Fig. 3e, blue) of the original curve  $\widehat{T}$  (Fig. 3e, green), such that the two curves connect smoothly at  $A = \Omega$  and  $M$  to form a closed two-period curve,  $\widehat{T}_2$ , enclosing an area  $S(r) = 2\pi r^2$ , thus obeying condition  $R_{A\Omega} = 1$ . This proves the TPT theorem. We make three remarks about this result.

- (1) Having property  $\pi$  is not obvious, because  $S(r)/r^2$  may often be a non-monotonic function of  $r$  (Fig. 3f and Extended Data Fig. 4e,h and figure captions). Also, property  $\pi$  is sufficient but not necessary for the existence of a TPT: for instance, a degenerate loop in which a flat curve is traversed forward and then in reverse, automatically yields a period-one trajectoid, and therefore a TPT as well. Alternative forms of property  $\pi$  are discussed in the Methods.
- (2) The TPT theorem proof implies, in particular, that splitting the trajectoid through the plane of the great arc  $\widehat{U}$  produces two identical halves: we illustrate this twofold rotational symmetry in Supplementary Video 2 (first experiment) with a trajectoid built from



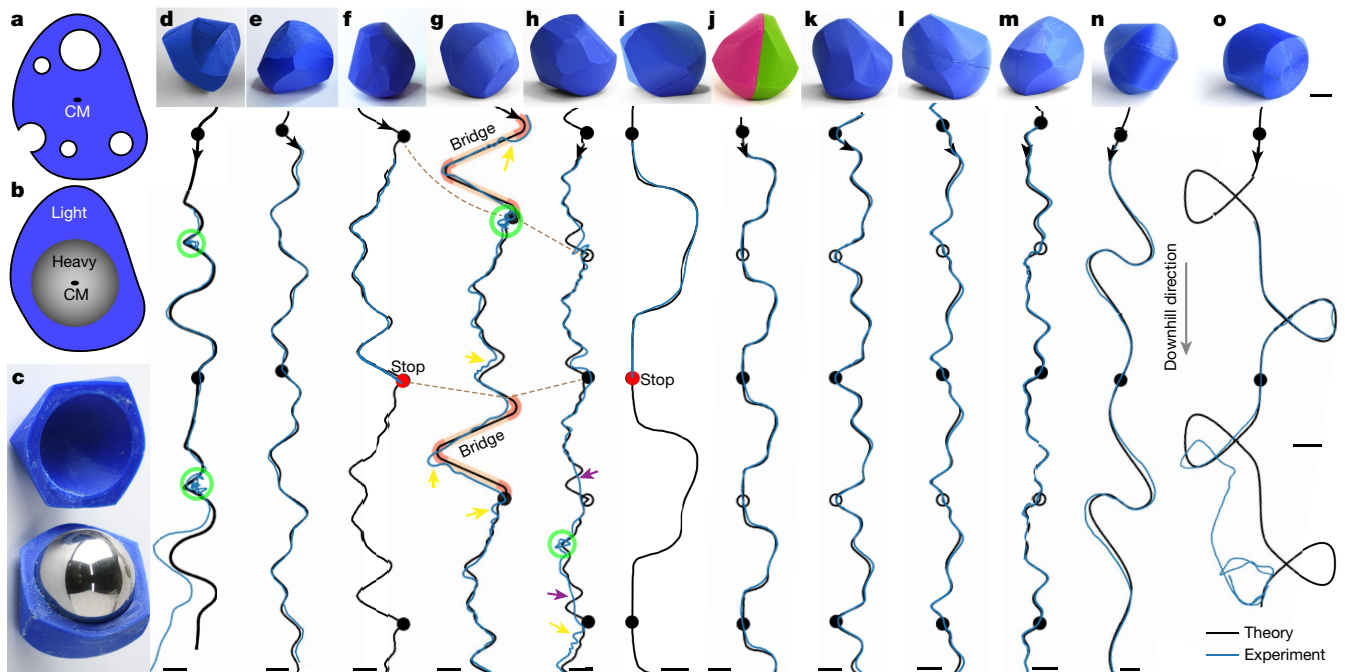


**Fig. 4 | Experimental validation.** **a, b**, Methods of CM engineering: introducing strategically placed voids (**a**) or using a heavy sphere concentric with the desired location of the CM (**b**). **c**, Photograph of two three-dimensionally printed halves of one shape, each containing a hemispherical void for housing a steel ball bearing (1-inch diameter). **d–o**, Examples of specific paths and corresponding bodies. Solid black lines are intended trajectories of the CM. Blue curves are experimental trajectories obtained by image-processing of top-view experimental videos (Methods and Supplementary Video 2). Filled black (or black and red in **f**) markers denote locations corresponding to the body's single revolution. The smallest period is between any two adjacent black circles (empty or filled). Green circles highlight sharp corners at which tumbling or recoiling was observed. Yellow arrows point to slight zig-zag wiggling of the experimental trajectory around the intended path. **d, e**, Examples of

single-period,  $n = 1$  trajectoids of strictly downhill paths. **f, i**, Examples of paths that have no single-period trajectoid; the body shaped to match this path stops after one period at the point marked red. **g**, However, the single-period trajectoid exists for a path similar to **f** but with a bridge (orange) appended to it. **h**, Alternatively, the input path from **f** can be traced by a two-period,  $n = 2$  trajectoid. Correspondence to **f** and **g** is emphasized by brown dashed lines. Along path **h**, the trajectoid gains enough kinetic energy to cut some corners (for example, purple arrows) and occasionally escape the main potential trench illustrated in Extended Data Fig. 7c. **j, m**, Further  $n = 2$  trajectoids. The trajectoid in **j** is manufactured from two identical halves (magenta and green) corresponding to two periods (symmetry axis OC in Fig. 3e). **n, o**, The  $n = 1$  trajectoids that roll, respectively, intermittently upwards and in loops. Scale bars are 1 cm. Each experiment was replicated at least 5 times.

such halves (Fig. 4j). Generalizing this construction to  $n$ -fold symmetry, we prove that multi-period trajectoids (MPT) with any  $n > 1$  exist for paths having property  $2\pi/n$  (MPT theorem in the Methods).

- (3) Property  $\pi$  is obeyed by a rich variety of unusual paths, including self-intersecting, spiralling and two-dimensional random walk paths shown in Extended Data Fig. 4. On the other hand, there exist special paths that violate property  $\pi$ . A simple example is a symmetric, V-shaped path with an acute angle between the equal arms (Extended Data Fig. 5a–c and Supplementary Video 4) or some more complex V-like paths with perfect symmetry of the arms (Extended Data Fig. 5d and further details in Methods). Because of this extra symmetry, they are much rarer than paths having property  $\pi$ . Also note that any slightest tapering of the acute angle of V-shaped path already gives it property  $\pi$  (Extended Data Fig. 5g). Although we cannot prove that these are the only paths that violate property  $\pi$ , we conjecture that paths without property  $\pi$  are infinitely rare, because they never appeared among random paths in our numerical experiments.

## Experimental validation

Turning to the experimental validation of the algorithm, we recall that the location of the trajectoid's CM was assumed to be insensitive to the final shape itself, and so the CM of the manufactured object must be at this predefined point  $C_M$ . This can be achieved in several ways.

For example, voids can be strategically introduced into the design of a three-dimensionally printed object<sup>22,23</sup> (Fig. 4a), including voids that reach the surface: these would not affect the rolling as long as they do not influence the shape's convex hull. Instead, we simply placed a heavy 1-inch (2.54 cm) ball bearing (steel,  $\rho = 7.8 \text{ g cm}^{-3}$ ) into a spherical cavity centred on  $C_M$  (Fig. 4b) inside a trajectoid made of a light,  $\rho = 1.25 \text{ g cm}^{-3}$ , polylactic acid (PLA). As shown in the image in Fig. 4c, we three-dimensionally printed the shape in two halves, each one having a hemispherical cavity for the steel ball, and glued them together after the ball was inserted. The shape of the PLA shell was determined by the shaving procedure described earlier (Fig. 1) and implemented numerically as described in the Methods. Readers can do it for a path of their own by using the online Google Colab notebook released with this paper. We used the  $R/r$  value of 1.3 to ensure adequate depth of the potential energy groove (Fig. 1 and Extended Data Fig. 1a) and better stability along the path. Overall, this fabrication scheme ensured that our trajectoids were heavy despite the low density of the PLA part, which is experimentally convenient as it makes gravity dominant relative to stray forces of other nature. Furthermore, it makes rotational inertia more isotropic, with moments of inertia dominated by those of the heavy steel ball.

The fabricated trajectoids were released to roll down a flat plane inclined at angles  $0.6$ – $1.7^\circ$ , with the instantaneous locations of the centre of gravity estimated and tracked (Methods). Figs. 4d, e, n, o and Extended Data Fig. 6a, b show the trajectories traced by one-period ( $n = 1$ ) trajectoids. As seen, there is generally close correspondence



between the intended and experimental results, save for some wiggling at sharp corners that is due to non-zero inertia of the physical bodies (if the trajectoid loses too little energy to friction and inelastic collisions, its total energy might eventually become sufficient for escaping the potential trench that follows the target path; see the last two periods in Fig. 4h and Supplementary Videos 1 and 2). Next, Fig. 4f,i shows bodies for which the single-period path  $T$  mapped onto the sphere does not close up: as predicted, the rolling for such a body is not periodic and it stops after one period (red dot). However, a trajectoid can be constructed when  $T$  is either corrected by adding a bridge (orange colour in Fig. 4g) or when, in accordance to TPT theorem, two periods  $T$  are used ( $n = 2$  trajectoids in Fig. 4h,j). More examples of  $n = 2$  trajectoids are shown in Figs. 4j–m. Apart from being a source of local wiggling, inertia can be harnessed to follow trajectories that intermittently roll upwards (Fig. 4n) or even in loops (Fig. 4o). Although the energy of a downward-rolling object decreases owing to friction, its kinetic component (inertia) may be sufficient to climb along the potential groove yet insufficient to escape it (Extended Data Fig. 7). In practice, such trajectoids performed reliably only for sufficiently smooth paths, because recoils and oscillations near sharp turns render the energy loss stochastic and thereby the progression along the periods unpredictable.

## Extensions and outlook

The TPT theorem is a universal property of rotations that can be translated from trajectoids to other physical systems governed by the rotation group  $SO(3)$ . In quantum-mechanical systems, the overall rotation  $R_{A\Omega}(2)$  can be seen as a time-evolution operator,  $U_{A\Omega} = \mathcal{T}\{\exp[-(i/\hbar)\int_A^{\Omega} dt H(t)]\}$ , with a time-dependent Hamiltonian  $H(t) \sim \mathbf{n}(t) \cdot \mathbf{L}$  and a time-varying field  $\mathbf{n}(t)$ . Notable examples are a magnetic dipole in a planar magnetic field<sup>24</sup> and the Bloch sphere representation of a qubit driven by an electric field<sup>25–27</sup> (Extended Data Fig. 9a and Methods). By ‘almost any’ rotation sequences we henceforth mean those having property  $\pi$ . The TPT theorem suggests that almost any planar field pulse  $\mathbf{n}(t)$ , once scaled by an appropriate factor  $r > 0$  and applied twice in a row, will return the system exactly to its original state,  $U_{A\Omega} = 1$ . Such  $360^\circ$ -rotation pulses play a role in common pulse sequences, as found in rotary echo<sup>28,29</sup> and Wimperis sequences<sup>30</sup>, and the TPT theorem may inspire a new sequence design for nuclear magnetic resonance (NMR)<sup>16</sup>, atom interferometry<sup>31</sup> or verification of quantum simulators<sup>32</sup>. The scaling factor  $r$  can be interpreted as modulating the magnitude of the pulse,  $\mathbf{n}(t) \rightarrow \mathbf{n}(t)/r$ , or as stretching it in time,  $\mathbf{n}(t) \rightarrow \mathbf{n}(tr)$  (Extended Data Fig. 9b,c and Supplementary Video 5). In this analogy, very small trajectoids,  $r \rightarrow 0$ , represent the adiabatic limit, where the field  $\mathbf{n}(tr)$  changes very slowly relative to the revolutions of the state vector: to such a tiny rolling trajectoid, smooth paths seem straight and therefore trace great circles on the core ball (Fig. 2), such that the trajectoid becomes a cylinder (shown in Supplementary Video 8, Extended Data Fig. 10 and Methods).

In classical optics, the evolving state vector can be taken as polarization vector of light rotating on the Poincaré sphere (Extended Data Fig. 9d). When light passes through a thin uniaxial waveplate, its polarization vector rotates by an angle proportional to the plate’s thickness  $\delta t$ , around a planar axis  $\mathbf{n} = (\cos\psi, \sin\psi, 0)$  (refs. 33,34), where  $\psi/2$  is the angle of the waveplate’s optical axis (Extended Data Fig. 9e and Methods). Here, the TPT theorem implies that for almost any given sequence of waveplates—with arbitrary thicknesses  $\delta t_i$  and optical axis directions  $\psi_i/2$ —there exists a scaling factor  $r$  such that any light entering the doubled sequence of waveplates with thicknesses  $\delta t_i/r$  regains its original polarization when it exits (Extended Data Fig. 9e–g and Supplementary Video 6). This basic property may become another tool in an optical designer’s toolbox, perhaps an aid in creating polarization-insensitive (‘phase-only’) optical devices based on liquid

crystal electro-optic effects for LIDAR (laser imaging, detection and ranging) and holographic displays<sup>35–37</sup>.

Further examination of the basic geometric problem of trajectoids may lead to unexpected analogies and applications in other physical settings, for example, when the trajectoids in time-varying driving field (for example, magnetic<sup>12,13</sup>) could be used to achieve complex motions with fewer moving parts and inside sealed spaces. Moreover, trajectoids morphing on-the-fly by means of piezoelectric actuators for solids<sup>38</sup> or gas inflation of soft hollow shapes<sup>39</sup> could be useful in robotics.

## Online content

Any methods, additional references, Nature Portfolio reporting summaries, source data, extended data, supplementary information, acknowledgements, peer review information; details of author contributions and competing interests; and statements of data and code availability are available at <https://doi.org/10.1038/s41586-023-06306-y>.

- Dirnböck, H. & Stachel, H. The development of the oloid. *J. Geom. Graph.* **1**, 105–118 (1997).
- Hirsch, D. A device for generating a meander motion. Patent no. 59720 (1980).
- Phillips, D. & Seaton, K. A. The polycons: the sphericon (or tetracon) has found its family. *J. Math. Arts* **14**, 345–359 (2020).
- Seaton, K. & Hirsch, D. Platonicons: the platonic solids start rolling. In *Proc. Bridges 2020: Mathematics, Art, Music, Architecture, Education, Culture* (eds Yackel, C. et al.) 371–374 (Tessellations Publishing, 2020).
- Stewart, A. T. Two-circle roller. *Am. J. Phys.* **34**, 166–167 (1966).
- Phillips, A. Meander mazes on polysphericons. In *The Visual Mind II* (ed. Emmer, M.) 667–684 (MIT Press, 2005).
- Muramatsu, T. The construction of a rideable geometric object based on a conical form: regarding ‘space walk on the earth’ with ellipsoidal rolling plane. *J. Geom. Graph.* **15**, 203–212 (2011).
- Kuleshov, A. S., Hubbard, M., Peterson, D. L. & Gede, G. Motion of the oloid on the horizontal plane. *Russ. J. Nonlinear Dyn.* **7**, 825–835 (2011).
- Bäsel, U. & Dirnböck, H. The extended oloid and its contacting quadrics. *J. Geom. Graph.* **19**, 161–177 (2015).
- Schatz, P. *The Study of Rhythms and Technology: The Evertible Cube. Polysomatic Form-Finding* (Niggli, 2013).
- OLOID Solution GmbH. OLOID—Technology. OLOID <https://www.oid.de/index.php/en/procedures> (2021).
- Jeon, S. Self-positioning ability of a sphericon-shaped magnetic millirobot rolling on an inclined surface. *AIP Adv.* **8**, 056729 (2018).
- Jeon, S. A sphericon-shaped magnetic millirobot rolling on a surface actuated by an external wobbling magnetic field. *AIP Adv.* **7**, 056708 (2017).
- Rhodes, T., Gotberg, C. & Vikas, V. Compact shape morphing tensegrity robots capable of locomotion. *Front. Robot. AI* <https://doi.org/10.3389/frobt.2019.00111> (2019).
- Haller, J. I. & Samija, L. The moving OLOID—a different pet in different times. *Autodesk Instructables* <https://www.instructables.com/The-Moving-OLOID-a-Different-Pet-in-Different-Time/> (2020).
- Merrill, J. T. & Brown, K. R. Progress in compensating pulse sequences for quantum computation. In *Quantum Information and Computation for Chemistry* (ed. Kais, S.) 241–294 (John Wiley & Sons, Ltd, 2014).
- Chirikjian, G. S. *Stochastic Models, Information Theory, and Lie Groups* Vol. 1, 155–159 (Birkhäuser, 2009).
- Kobayashi, S. *Differential Geometry of Curves and Surfaces* (Springer, 2021).
- Segerman, H. Rolling acrobatic apparatus. *Not. Am. Math. Soc.* **68**, 1 (2021).
- Dyson, F. J. The S matrix in quantum electrodynamics. *Phys. Rev.* **75**, 1736–1755 (1949).
- Levi, M. Geometric phases in the motion of rigid bodies. *Arch. Ration. Mech. Anal.* **122**, 213–229 (1993).
- Prévost, R., Whiting, E., Lefebvre, S. & Sorkine-Hornung, O. Make it stand: balancing shapes for 3D fabrication. *ACM Trans. Graph.* **32**, 1–10 (2013).
- Bächer, M., Whiting, E., Bickel, B. & Sorkine-Hornung, O. Spin-it: optimizing moment of inertia for spinnable objects. *ACM Trans. Graph.* **33**, 96 (2014).
- Rojo, A. G. & Bloch, A. M. The rolling sphere, the quantum spin, and a simple view of the Landau–Zener problem. *Am. J. Phys.* **78**, 1014–1022 (2010).
- Feynman, R. P., Vernon, F. L. & Hellwarth, R. W. Geometrical representation of the Schrödinger equation for solving maser problems. *J. Appl. Phys.* **28**, 49–52 (1957).
- Shore, B. *Manipulating Quantum Structures using Laser Pulses* 146–150 (Cambridge Univ. Press, 2011).
- Cohen-Tannoudji, C., Dupont-Roc, J. & Grynberg, G. *Atom—Photon Interactions: Basic Process and Applications* 353–363 (Wiley-VCH, 1998).
- Butts, D. L., Kinast, J. M., Timmons, B. P. & Stoner, R. E. Light pulse atom interferometry at short interrogation times. *J. Opt. Soc. Am. B* **28**, 416 (2011).
- Rakreungdet, W. et al. Accurate microwave control and real-time diagnostics of neutral-atom qubits. *Phys. Rev. A: At. Mol. Opt. Phys.* **79**, 022316 (2009).
- Wimperis, S. Broadband, narrowband, and passband composite pulses for use in advanced NMR experiments. *J. Magn. Reson. A* **109**, 221–231 (1994).
- Dunning, A. et al. Composite pulses for interferometry in a thermal cold atom cloud. *Phys. Rev. A* **90**, 033608 (2014).

32. Shaffer, R., Megjedish, E., Broz, J., Chen, W.-T. & Häffner, H. Practical verification protocols for analog quantum simulators. *npj Quantum Inf.* **7**, 46 (2021).
33. Chekhova, M. & Banzer, P. *Polarization of Light: in Classical, Quantum, and Nonlinear Optics* (Walter de Gruyter GmbH & Co KG, 2021).
34. Svirko, Y. P. & Zheludev, N. I. *Polarization of Light in Nonlinear Optics* (Wiley, 1998).
35. Liu, J. & Wang, J. Demonstration of polarization-insensitive spatial light modulation using a single polarization-sensitive spatial light modulator. *Sci. Rep.* **5**, 9959 (2015).
36. Li, S.-Q. et al. Phase-only transmissive spatial light modulator based on tunable dielectric metasurface. *Science* **364**, 1087–1090 (2019).
37. Xiong, J., Hsiang, E.-L., He, Z., Zhan, T. & Wu, S.-T. Augmented reality and virtual reality displays: emerging technologies and future perspectives. *Light: Sci. Appl.* **10**, 216 (2021).
38. Wu, Y. et al. Insect-scale fast moving and ultrarobust soft robot. *Sci. Robot.* **4**, eaax1594 (2019).
39. Walker, J. et al. Soft robotics: a review of recent developments of pneumatic soft actuators. *Actuators* <https://doi.org/10.3390/act9010003> (2020).

**Publisher's note** Springer Nature remains neutral with regard to jurisdictional claims in published maps and institutional affiliations.

Springer Nature or its licensor (e.g. a society or other partner) holds exclusive rights to this article under a publishing agreement with the author(s) or other rightsholder(s); author self-archiving of the accepted manuscript version of this article is solely governed by the terms of such publishing agreement and applicable law.

© The Author(s), under exclusive licence to Springer Nature Limited 2023

### Numerical calculation of the tractoid shape

Once we approximate the planar path  $A\Omega$  by a polygon made of short line segments of length  $\delta t$ , as described in the main text, the matrix  $R_{k \leftarrow 0}$  for rotation from the start of the path ( $t_0 = 0$ ) to the position  $t_k$  is a product:

$$R_{k \leftarrow 0} = \prod_{i=1}^k R_i = R_k \cdots R_2 R_1 \quad (3)$$

The removal of a shell fragment (shaving) is performed by applying Boolean mesh operations to subtract a series of cubes  $C_k = (R_{k \leftarrow 0})^{-1}C$  from the initially geodesic mesh of the shell that envelopes (and is concentric with) the core sphere. The inverse rotations slide the cube along the spherical path, instead of rotating the core with respect to  $C$ . Meshes of the cubes  $C_k$  were produced with Python by rotations of a cube  $C$  whose position and orientation are shown in Extended Data Fig. 1b, then the  $C_k$  were imported into Autodesk 3ds Max 2018 (ref. 40) for executing standard Boolean mesh operations, although any other 3D CAD software would also be suitable for the purpose. Readers can supply their intended paths to the online Google Colab notebook released with this paper (Code availability statement at the end of the paper) to calculate tractoid shapes.

### Fabrication

After the tractoid's shape was calculated numerically as described above and using parameters  $r = 15.88$  and  $R = 20.64$  mm, three-dimensional (3D) printing of calculated shape was performed with PLA on Ultimaker 3 Extended printer (Ultimaker B.V.) with triangular infill at 50% density (generated by Ultimaker Cura slicer). To ensure that the CM of the manufactured object was always at the predefined point (CM in Fig. 1c), a heavy steel ball (diameter 2.54 cm or 1 inch =  $1.6r$ ) was placed into a spherical cavity centred on CM (Extended Data Fig. 1d and Fig. 4c). As shown in Fig. 4c, the tractoid was three-dimensionally printed in two halves, each having a hemispherical cavity for the steel ball. After the ball was inserted, the halves were glued together with cyanoacrylate (Loctite) glue. This approach yielded a heavy object despite the low density of the 3D-printing material (PLA) and ensured that gravity dominated stray forces of different natures. Furthermore, it made rotational inertia more isotropic, with moments of inertia dominated by those of the heavy steel ball.

### Analysis of experimental trajectories

Silicon carbide abrasive paper (electro-coated, 2000Cw) was glued onto a sloped 12-mm-thick glass slab to prevent slippage and pivoting during rolling. Slope angle and direction were measured by high-precision, two-axis digital inclinometer (Dong-Do IM-2DT). Videos were acquired at either 60 or 120 frames per second using a digital camera (D850, Nikon) placed 1.62 m above the slope. The centroid of the object's apparent projection on the top-view videos was found by thresholding the red, green, blue values of video frames to detect the projection outline. Before finding the centroid, a convex hull operation was applied to the detected projection to eliminate any possible non-convexity: as the object's shape is convex by construction, its projection must be convex. To evaluate whether the centroid of the visible shape can be used as an adequate estimate of the object's CM location, we simulated shape projections of the tractoid onto the plane as it rolled along the target path. We then compared the trajectory of the simulated projection centroid (orange solid lines in Extended Data Fig. 8a–c) to the target path, that is, to the theoretical trajectory of projection of the CM onto the plane (black solid lines in Extended Data Fig. 8a–c). The difference between these two trajectories was found to be negligible. Furthermore, for tractoids of paths as in Extended Data Fig. 9a,c, the planar distance between the projection of the CM and the centroid of the shape

projection never exceeds 8.7% of the tractoid's minimal radius  $r = 1$  for all possible orientations of the tractoid (Extended Data Fig. 8d,f).

Note 1: the location of the CM can also be estimated more precisely by applying the standard algorithms of six-degree-of-freedom (6D) pose (position and orientation) tracking to the experimental video: these algorithms yield global location and orientation of the solid's own reference frame, in which location of the true CM is known a priori. To test this method, we applied markers to the surface of a manufactured tractoid (black dots in Extended Data Fig. 8e), filmed its rolling at 120 frames per second and applied 6D pose estimation algorithms of the Blender software<sup>41</sup> (Supplementary Video 6). Data presented in Extended Data Fig. 8h,i evidenced that the 6D pose approach produces only a negligible improvement of precision as compared to the shape centroid method described above.

Note 2: the symmetry of the two halves of the TPT is illustrated at the beginning of Supplementary Video 2 with a two-colour tractoid. However, only one-colour tractoids were used for analysis of experimental trajectories.

### Path integral form of the $R_{A\Omega} = 1$ condition

For an infinitesimal path segment  $dt$ , the rotation matrix can be written in terms of the rotation group generators:  $R(\mathbf{n}(t), dt/r) = e^{(dt/r)(\mathbf{n} \cdot \mathbf{L})} = 1 + (dt/r)(\mathbf{n} \cdot \mathbf{L})$ . Hence, the matrix of net accumulated rotation after rolling along the entire period  $A\Omega$  is a product integral,

$$R_{A\Omega} = \prod_{t=A}^{\Omega} R\left(\mathbf{n}(t), \frac{dt}{r}\right) = \prod_{t=A}^{\Omega} e^{\frac{dt}{r}(\mathbf{n}(t) \cdot \mathbf{L})} = \prod_{t=A}^{\Omega} \left[1 + \frac{dt}{r}(\mathbf{n}(t) \cdot \mathbf{L})\right],$$

where each further rotation matrix is multiplied from the left-hand side. Equivalently, one can write a path-ordered exponential,

$$R_{A\Omega} = \mathcal{T} \left[ \exp \left( \frac{1}{r} \int_A^{\Omega} dt \mathbf{n}(t) \cdot \mathbf{L} \right) \right] \quad (4)$$

where the time-ordering operator  $\mathcal{T}$  makes sure that the rotations and the generators are multiplied in the correct order according to their positions along the path. This compact form links the tractoids to the basic concept of propagators and path integrals of quantum field theory<sup>20</sup>. In this language, the tractoid existence condition means that the time-evolution operator in equation (2) is equal to the unity rotation  $R_{A\Omega} = 1$ .

### Further considerations for the proof of the TPT theorem

Here, we give the proof for a simple path  $T = AM$ , which, in the plane, has the same tangent direction at the beginning and the end, such that the integral  $I_T$  of the curvature (1) vanishes modulo  $2\pi$ . When the curve is mapped onto the sphere, the beginning and end points are mapped to two points  $A$  and  $M$  and we draw the geodesic arc from  $M$  to  $A$  (the shorter of the two). By property  $\pi$  discussed in the main text, there exists a radius  $r$  of the sphere, for which the area enclosed by the curve and the arc is exactly  $\pi r^2$ . By the Gauss–Bonnet theorem, the (interior) angles at  $A$  and  $M$  add up to  $2\pi - (\text{enclosed surface})/r^2 = \pi$ . Because the tangents at  $A$  and  $M$  in the plane are the same, the exit angle at  $M$  is equal to the entry angle at  $A$ , as illustrated in Fig. 3e. It follows that on rolling over the second period, the graph on the sphere  $M\Omega$  is the same as the first, but now turned by  $180^\circ$ . Therefore, the area enclosed by the second part is again  $\pi r^2$  and the sum is  $2\pi r^2$ , which is half the area of the sphere. This means that the  $R_{A\Omega} = 1$  condition is satisfied, and therefore the tractoid will be in exactly the same orientation as when it started at  $A$ , once it has rolled over two copies of the original path. The path can be continued indefinitely. For the more general cases, the argument is the same, taking into account that the tangents at  $A$  and  $M$  might be unequal, and that the areas might overlap, in which case the orientation of the curvature will come into play. For an animated illustration of this proof, see Supplementary Video 3.



## Paths without property $\pi$

Let us consider a path consisting of just two straight segments whose normals are  $\mathbf{n}_1$  and  $\mathbf{n}_2$ , such that the sphere undergoes just two rotations: around axes  $\mathbf{n}_1$  and  $\mathbf{n}_2$  by angles  $\alpha\sigma$  and  $\beta\sigma$  where  $\alpha$  and  $\beta$  are arbitrary positive fixed values and  $\sigma > 0$  is the scaling factor. The rotation angle of the composition of the two rotations is equal to  $\pi$  if and only if<sup>42</sup>

$$\cot(\alpha\sigma/2)\cot(\beta\sigma/2) = \mathbf{n}_1 \cdot \mathbf{n}_2 \quad (5)$$

If  $\alpha \neq \beta$ , a solution  $\sigma > 0$  of equation (5) always exists, because in this case the right-hand side of equation (5) is limited to an interval  $[-1, 1]$ , but the left-hand side spans  $(-\infty, \infty)$ . If  $\alpha = \beta$ , the left-hand side of equation (5) is positive—spans  $(0, \infty)$ —for all  $\sigma > 0$  and equation (5) can only be satisfied for  $\mathbf{n}_1 \cdot \mathbf{n}_2 \geq 0$  and has no solutions if  $\mathbf{n}_1 \cdot \mathbf{n}_2 < 0$ .

Supplementary Video 4 and Extended Data Fig. 5 explore paths that are similar to acute-angle isosceles V paths. We found that an acute-angle symmetric V-like path still does not have property  $\pi$  even after we introduce a kink into the arms of V-path at points  $K_1$  and  $K_2$  as shown in Extended Data Fig. 5d: note that  $S(\sigma)$  plot in Extended Data Fig. 5e never reaches  $\pi$  or  $-\pi$ . Sweep of the kink angle  $\alpha$  is shown in Supplementary Video 4. At the same time, introducing a slightest taper at the corner of the V-path, as shown in Extended Data Fig. 5g, produces a path that has property  $\pi$ : solution of  $S(\sigma) = \pi$  is marked by the red dot in Extended Data Fig. 5h. Furthermore, deviation from the perfect symmetry of the V-like path's arms (Extended Data Fig. 5k) also produces a path that has property  $\pi$ : the function  $S(\sigma)$  reaches  $-\pi$  (red dot in Extended Data Fig. 5l). Asymmetry in the last example is controlled by a parameter  $\Xi$  responsible for the difference between kink angles  $\alpha$  and  $\beta$  in two arms:  $\beta = \alpha(1 + \Xi)$  as shown in Extended Data Fig. 5k. The sweep of asymmetry  $\Xi$  is shown in Supplementary Video 4.

Last, we discuss a version of how one could define rare paths. We have shown that certain piecewise linear functions, with some extra symmetry, define paths for which neither one nor TPTs exist. Clearly, the space of such functions has finite dimension, whereas the functions of differentiability class  $C^1$  considered above form an infinite dimensional space. However, there might be other curves for which no TPT exists, and we leave this as an open question. Apart from examples such as those in Extended Data Fig. 5a,d, numerical experimentation yielded no other curves without TPTs, and so we conjecture that there may be none.

## Generalization of the TPT theorem to MPT

For any  $n \geq 2$ , we prove the following theorem:

### MPT theorem

The  $n$ -period trajectoids can be constructed for paths  $T_\infty$  whose period  $T$  has the following property  $2\pi/n$ : as a sphere of finite radius  $r > 0$  rolls along the period  $T = AM$ , the contact point traces on the sphere's surface a curve  $\widehat{T}$  (which is generally not closed; green in Extended Data Fig. 1c,d).  $\widehat{T}$  can then be closed by an isosceles V-shaped wedge made of two great arcs  $\widehat{M\Lambda\Lambda}$  (red in Extended Data Fig. 1c,d), with an angle  $2\pi/n$  at  $\Lambda$  (orange angle in Extended Data Fig. 1c). Together,  $\widehat{T}$  and the wedge  $\widehat{M\Lambda\Lambda}$  connecting its ends enclose some oriented spherical area  $S(r)$  (shaded green in Extended Data Fig. 1c,d). The condition requires that there exists an  $r$  for which  $S(r)/r^2 = \pm 2\pi/n$ .

The proof again uses the Gauss–Bonnet theorem: the area having property  $2\pi/n$  is  $S(r)/r^2 = 2\pi/n = 2\pi - \oint dt \kappa(t)$ . However, the curvature's integral vanishes along  $\widehat{T}$  (by periodicity, equation (1)), and along the two big arcs of  $\widehat{M\Lambda\Lambda}$  (as these are geodesic), so the only remaining contribution comes from the corners with their angles,  $\alpha$  at  $A$ ,  $\lambda = 2\pi/n$  at  $\Lambda$  and  $\mu$  at  $M$ :  $2\pi/n = 2\pi - [(\pi - \alpha) + (\pi - \lambda) + (\pi - \mu)] = 2\pi/n + (\alpha + \mu - \pi)$ . It follows that, for any  $n \geq 2$ , the two side corners of the wedge add up to  $180^\circ$ ,  $\alpha + \mu = \pi$ . This allows us to draw  $n$  copies of  $\widehat{T}$ ,  $i = 1, \dots, n$  (blue and yellow in Extended Data Fig. 1c, also magenta and sky-blue in

Extended Data Fig. 1d), each rotated by an angle  $2\pi i/n$  around  $O\Lambda$  with respect to the original  $\widehat{T}$ , such that all  $n$  paths connect smoothly to form a closed  $n$ -period path,  $\widehat{T}_n$ , enclosing an area  $S(r) = 2\pi r^2$ , thus obeying condition  $R_{A\Omega} = 1$ , which proves the MPT theorem. The corresponding trajectoid will show  $n$ -fold rotational symmetry and can therefore be assembled from  $n$  identical parts. The case  $n = 2$  corresponds to the TPT theorem and property  $\pi$ , where the wedge becomes a single great arc. For  $n = 1$ , the arc vanishes and  $T$  must be closed with property  $2\pi$ , which is simply the Gauss–Bonnet form of condition  $R_{A\Omega} = 1$ .

In the context of ref. 19, the property  $2\pi/n$  says that the holonomy (change in the orientation and position of the trajectoid with respect to the plane) is a pure translation after having covered exactly  $n$  copies of the original path.

Because of the limits  $\lim_{r \rightarrow \infty} S(r)/r^2 = 0$  and  $\lim_{n \rightarrow \infty} 2\pi/n = 0$ , one may be tempted to prove that for any given  $T$ , there exists a large enough  $n$  such that an  $n$ -period trajectoid exists for  $T$ . The obstacle to such attempts is the discontinuity of  $S(r)$  for  $n > 2$ . Note that the above mentioned  $\widehat{M\Lambda\Lambda}$  can be constructed only when the arc length  $\widehat{M\Lambda}$  is not larger than  $2\pi r/n$ . This can be seen from the spherical rule of cosines applied to the spherical triangle  $M\Lambda\Lambda$ ,  $\cos \frac{\widehat{M\Lambda}}{r} = \cos \frac{2\widehat{M\Lambda}}{r} + \sin^2 \frac{\widehat{M\Lambda}}{r} \cos \frac{2\pi}{n} \geq \cos \frac{2\pi}{n}$  and therefore we find  $\widehat{M\Lambda} \leq 2\pi r/n$ , where equality applies only when  $\widehat{M\Lambda} = \widehat{A\Lambda} = \pi r/2$ . As a consequence,  $S(r)$  is not a continuous function of  $r$ : it is undefined when  $\widehat{M\Lambda} > 2\pi r/n$ . In practice, this means that increasing  $n$  typically reduces the domain of  $S(r)$ . It is also noteworthy that  $S(r)$  is multivalued: whenever  $\widehat{M\Lambda\Lambda}$  can be constructed, it can be constructed in two different ways that are mirror reflections of each other in the plane  $AMO$ . This ambiguity allows  $S(r)$  to have two values for each  $r$  in its domain.

Following the example of the TPT, we find that counterexamples to property  $2\pi/n$  are also single isosceles V paths, with corners  $\gamma$  sharper than  $\pi/n$  (generalizing the TPT case,  $\gamma < \pi/2$  where  $n = 2$ ). To show that these are counterexamples, note that for V to have property  $2\pi/n$ , rolling along one V must give a matrix of rotation by an angle  $2\pi/n$  around some axis. Then, using the formula for the composition of two rotations with  $\alpha = \beta$  to obtain the rotation angle  $2\pi/n$  requires:

$$\begin{aligned} \cos(\pi/n) &= \cos^2(\alpha\sigma/2) - \sin^2(\alpha\sigma/2)(\mathbf{n}_1 \cdot \mathbf{n}_2) \\ &= \cos^2(\alpha\sigma/2) + \sin^2(\alpha\sigma/2)\cos\gamma \\ &\geq \cos^2(\alpha\sigma/2)\cos\gamma + \sin^2(\alpha\sigma/2)\cos\gamma = \cos\gamma \end{aligned}$$

However, for any  $\gamma < \pi/n$ , we find a contradicting inequality,  $\cos(\pi/n) < \cos\gamma$ . It follows that such a V-shaped path with  $\gamma < \pi/n$  violates property  $2\pi/n$ .

## Bridging and scaling paths to support one-period trajectoids

Paths  $T$  typically do not satisfy condition  $R_{A\Omega} = 1$  for one-period ( $n = 1$ ) trajectoids and, consequently, the corresponding one-period trajectoids are rare. Still, one can find a path similar to the given one that allows for a one-period trajectoid. We developed two methods to achieve this: either by appending a specially constructed 'bridge' to the given path, or by deforming the given path itself. In both approaches, the quantity to minimize is the angle  $\theta$  of mismatch between the initial and final orientations of the sphere on completing one path period  $T$ . This angle is computed from Euler's axis-angle representation of the overall rotation matrix

$$\theta = \arccos\left(\frac{\text{tr } R_{A\Omega} - 1}{2}\right), \quad (6)$$

where  $\text{tr}$  is the trace operator.

Deforming the input path was performed as follows. Keeping a constant  $r = 1$ , we applied non-uniform scaling to  $T$  with two scaling coefficients,  $k_x$  along the downward direction and  $k_y$  perpendicular to it. For an example path from Fig. 4d (same as path in Fig. 1a and Fig. 2a), the map of angle  $\theta(k_x, k_y)$  is shown in Extended Data Fig. 2a. Our goal

is then to find scaling factors  $(k_x, k_y)$  that give  $\theta$  closest to zero, as long as  $k_y$  is not too small, because there is always a degenerate solution with  $k_y = 0$ , which turns the curve into a straight line whose trajectoid is a cylinder, but this solution is of no interest. For the example in Extended Data Fig. 2, we required  $k_y > 0.5$ . In Extended Data Fig. 2a, there are two locations with small  $\theta$ . For the one in Extended Data Fig. 2b, the corresponding curve  $\widehat{T}$  traced on the surface of a rolling sphere does not self-intersect; by contrast, for the minimum in Extended Data Fig. 2c,  $\widehat{T}$  has many self-intersections.

If one needs a one-period trajectoid, deforming  $T$  by just two scaling factors in orthogonal directions is not always enough to fulfil  $R_{A\Omega} = 1$ . In practice, for some paths, no combination of  $k_x$  and  $k_y$  can yield  $\theta(k_x, k_y) < 2^\circ$  (a mismatch angle acceptable in light of the imperfections of our fabrication process). In these cases (Fig. 4d,e,n,o), we slightly adjusted the nodes of the Bezier spline through which the initial  $T$  was defined (shown in Extended Data Fig. 2e) and recalculated the  $\theta(k_x, k_y)$  map again (Extended Data Fig. 2d,f). Generally, global optimization algorithms must be used for such deformation of the input path, but, for instance, a path in Extended Data Fig. 2e needed just three to four iterations of adjustment to end up with a minimum value  $\theta(k_x, k_y) < 2^\circ$ .

Instead of deforming the input path, a special bridge may be appended to it such that a one-period trajectoid exists for the overall curve (input path plus the bridge). To improve the practical performance, we avoid using sharp corners in the bridge: curvature of bridge elements must not exceed certain  $\kappa_{\max}$ . The bridge thus consists of two straight arms (Extended Data Fig. 3, orange) connected to each other and to the ends of input path by arcs of curvature  $\kappa_{\max}$  (Extended Data Fig. 3, red). Each bridge is made to close the spherical trace of the overall curve (input path plus the bridge, Extended Data Fig. 3b). To ensure that trajectoid does not need to rely on inertia, straight sections of the bridge must always be directed ‘downhill’ with respect to the projection of gravity onto the plane (in Extended Data Fig. 3a taken to be from the left to the right). For a more robust practical performance, the elements of bridge must not self-intersect. Under all these constraints, for a given scale  $\sigma$  of the input path (for example, blue in Extended Data Fig. 3a,b), we construct a family of bridges shown in red and orange Extended Data Fig. 2b and parameterize by declination of arms (orange) away from the arc connecting the ends of the spherical trace of the scaled input path. In this family, we then find a bridge such that the overall spherical trace (of input path and the bridge together) splits the sphere into two spherical regions of equal area ( $2\pi r^2$ ) and by the Gauss–Bonnet theorem satisfies the  $R_{A\Omega} = 1$  condition. An example of such a solution is shown in Fig. 2c and validated experimentally in Fig. 4g. The entire algorithm begins with a value of  $\sigma$  giving the smallest possible distance between the ends of the input path’s spherical trace (Extended Data Fig. 3b, blue). If we are unable to find a proper bridge among the family of bridges for a given  $\sigma$ , we decrease  $\sigma$  and try again.

## Application of the TPT theorem in quantum and classical systems

Here, we illustrate how the TPT theorem can be translated from trajectoids to four other physical systems governed by the rotation group  $SO(3)$ : (1) magnetic dipoles in planar magnetic field, (2) NMR, (3) electric dipole transitions in a two-state quantum system under driving electric field, (4) the polarization state of light in classical optics. The Bloch sphere representation describes cases (2) and (3), and the closely related Poincaré sphere representation describes case (4). By almost any sequences, we henceforth mean those with property  $\pi$ .

(1) In a time-varying planar magnetic field  $B(t) = B(t)(\hat{x}\cos\psi(t) + \hat{y}\sin\psi(t))$ , a magnetic dipole moment rotates with instantaneous angular velocity  $\mathbf{n}(t) = -\gamma B(t)$ , where  $\gamma$  is the gyromagnetic ratio. The dynamics of a dipole in a field of constant magnitude ( $B(t) = B$ ) has been described<sup>24</sup> by rolling a sphere of radius  $r = 1/(\gamma B)$  along a flat curve that has  $\mathbf{n}(t)$  as its normal vector. A scale factor  $r$  can be applied in two ways: either to the field magnitude ( $B(t) \rightarrow B(t)/r$ ),

or by rescaling time ( $B(t) \rightarrow B(r)$ ). By the TPT theorem, almost any given  $B(t)$  can be scaled so that applying the scaled magnetic field twice, sequentially, brings any magnetic dipole back to the orientation it had before the experiment, whatever that orientation was.

(2) In the NMR context, a strong static magnetic field  $B_0$  along the  $z$  axis causes precession of the dipole moment around that axis with Larmor frequency  $\omega_0 = \gamma B_0$ , and a pulse of magnetic field  $B_1(t) = B_1(t)(\hat{x}\cos(\omega_0 t - \psi(t)) + \hat{y}\sin(\omega_0 t - \psi(t)))$  rotating in the  $xy$  plane is applied. For example, a linear increase of the phase shift  $\psi(t) = t\Delta$  will occur when the pulse is detuned slightly off-resonance<sup>25,26</sup>: that is, it oscillates with frequency  $(\omega_0 - \Delta)$  instead of  $\omega_0$ . If the phase shift  $\psi(t)$  and magnitude  $B_1(t)$  change slowly with time  $t$ , it is common to use the reference frame that rotates together with Larmor precession and formulate optical Bloch equations in a rotating wave approximation<sup>26,27</sup>, where state vector  $\rho(t)$  is the normalized magnetic dipole moment in the rotating frame, and its instantaneous angular velocity  $\mathbf{n}(t) = -\gamma B_1(t)[\hat{x}\cos\psi(t) + \hat{y}\sin\psi(t)]$  belongs to the  $xy$  plane. For the application of the TPT theorem, see the discussion after (3).

(3) The same Bloch sphere representation of state evolution applies also to the electric dipole transitions in a two-state quantum system under driving field  $E(t)\cos(\omega_0 t - \psi(t))$  near the resonant frequency  $\omega_0 = W/\hbar$ , where  $W$  is the energy difference between the two eigenstates. In this case, the state vector  $\rho(t)$  with unit length and components  $(u(t), v(t), w(t))$  (Extended Data Fig. 9a) is not in real space coordinates anymore: coordinates  $u$  and  $v$  are called ‘coherences’<sup>26</sup> and  $w$  is the population inversion<sup>25,26</sup>, which is equal to +1 and –1 for the system’s eigenstates (poles of the Bloch sphere in Extended Data Fig. 9a). Under applied driving field, the state vector  $\rho(t)$ , whose end is shown by a red circle in Extended Data Fig. 9a, has instantaneous angular velocity vector  $\mathbf{n}(t) = -\kappa E(t)(\hat{x}\cos\psi(t) + \hat{y}\sin\psi(t))$  (blue arrow in Extended Data Fig. 9a), where  $\kappa = \mu_{ab}/\hbar$  and  $\mu_{ab}$  is the transition dipole moment<sup>25</sup>. Rotation of  $\rho(t)$  is shown by an orange arrow in Extended Data Fig. 9a.

As in the case (1), in cases (2) and (3) a scale factor  $r$  can be applied either to the pulse magnitude ( $B_1(t) \rightarrow B_1(t)/r$ ,  $E(t) \rightarrow E(t)/r$ , green curves in Extended Data Fig. 9b,c and right side of Supplementary Video 5), or by stretching pulse functions in time ( $B_1(t) \rightarrow B_1(rt)$ ,  $E(t) \rightarrow E(r)$ ,  $\psi(t) \rightarrow \psi(rt)$ , blue curves in Extended Data Fig. 9b,c and left-hand side in Supplementary Video 5). By the TPT theorem, almost any given pulse can be scaled such that applying the scaled pulse twice brings the system back to the original state. Note that only the pulse envelope ( $B_1(t)$  or  $E(t)$ , dotted curve in Extended Data Fig. 9b) and phase shift curve  $\psi(t)$  (Extended Data Fig. 9c) must be copied and shifted in time by a delay  $L$ , but the carrier wave (at frequency  $\omega_0$ ) must be shared between the scaled copy and the scaled original: for example, if scaling is applied to the electric field magnitude, then the scaled shifted copy is  $(1/r)E(t-L)\cos(\omega_0 t - \psi(t-L))$  and the scaled original is  $(1/r)E(t)\cos(\omega_0 t - \psi(t))$ .

(4) In classical optics, the polarization state of light can be represented by a Stokes vector on the Poincaré sphere (Extended Data Fig. 9d), with purely circular polarizations at the sphere’s poles, on the  $S_3$  axis, and various linear polarizations in equatorial  $S_1, S_2$  plane. Consider a single thin uniaxial waveplate whose optic axis lies in the plane of the waveplate and forms angle  $\psi/2$  with the vertical axis of the global reference frame as shown for one of the waveplates in Extended Data Fig. 9e. When light of wavelength  $\lambda$  passes normally through such a waveplate of thickness  $\delta t$ , the Stokes vector on the Poincaré sphere rotates by an angle  $2\pi(n_e - n_o)\delta t/\lambda$  around the axis  $n$  (blue arrow in Extended Data Fig. 9d) that lies in the equatorial  $S_1, S_2$  plane (shaded blue in Extended Data Fig. 9d) at an angle  $\psi$  to the  $S_1$  axis<sup>33,34</sup>. Here,  $n_e - n_o$  is the difference of refractive indices between extraordinary and ordinary waves. Extended Data Fig. 9e shows a sequence of waveplates of various thicknesses and

orientations of optic axes (indicated by arrows). By the TPT theorem in this case, after scaling all thicknesses by an adequate factor  $1/r$  as illustrated in Extended Data Fig. 9f, and then doubling the sequence of waveplates as in Extended Data Fig. 9g, the resulting system will have no net effect on the polarization state of light passing through it. This analogy is illustrated in Supplementary Video 6.

### Small-radius limit of trajectoids

Consider a minute sphere rolling along a differentiable planar curve  $T$  with a geodesic curvature  $\kappa(t)$ . At the scale of the tiny sphere,  $r \rightarrow 0$  or  $\sigma \rightarrow \infty$ , the geodesic curvature vanishes,  $r\kappa(t) \rightarrow 0$ , such that  $T$  is effectively straight and the mapped curve on the sphere  $\widehat{T}$  is a geodesic, that is, a great circle (Extended Data Fig. 10a–c and Supplementary Video 8, 0:00–0:13). Therefore, the total 3D curvature of the spherical curve is  $\kappa_T = \sqrt{1/r^2 + \kappa(t)^2} \simeq 1/r$ . The path  $\widehat{T}$  will remain in the vicinity of the great circle and changes in the direction  $\kappa = d\psi/dt$  will only tilt it very slightly (Extended Data Fig. 10c). The resulting trajectoid is therefore a simple cylinder. Only the introduction of infinitely sharp corners, where  $\kappa_T = \kappa \rightarrow \infty$ , can make the curve markedly depart from the great circle. In a polygonal curve (Extended Data Fig. 10d), each smooth segment will be mapped to a great circle, and corners will induce transition among the circles (Extended Data Fig. 10e–g and Supplementary Video 8, 0:13–0:26).

### Data availability

All data in support of the findings of this study, including 3D shape files of demonstrated trajectoids, are available from a public repository: <https://doi.org/10.5281/zenodo.8116412>.

### Code availability

An online open-source demonstration on Google Colab allows users to design trajectoids for a path of their choice: [https://colab.research.google.com/drive/1XZ7Lf6pZu6nzEuqt\\_dUCHormeSbCCMIP](https://colab.research.google.com/drive/1XZ7Lf6pZu6nzEuqt_dUCHormeSbCCMIP). All Python code used to obtain results that are reported in the paper is available from a public repository: <https://doi.org/10.5281/zenodo.8116412>.

40. Autodesk 3ds Max (Autodesk, 2018).
41. Hess, R. *Blender Foundations: The Essential Guide To Learning Blender 2.6* (Focal Press, 2010).
42. Nielsen, M. A. & Chuang, I. L. *Quantum Computation and Quantum Information* 177 (Cambridge Univ. Press, 2010).

**Acknowledgements** This work was supported by the Institute for Basic Science, Republic of Korea, project code IBS-R020-D1 and by Swissmap (to J.-P.E.).

**Author contributions** Y.I.S. designed the algorithm that solves for trajectoid's shapes, implemented it in the software, fabricated the trajectoids, performed experiments, trajectory tracking and analysis. R.D. helped with experiments. T.T. and J.-P.E. developed the mathematical treatment. T.T. and Y.I.S. developed quantum-mechanical and classical analogies. S.G. and B.A.G. conceived and supervised research. Y.I.S., S.G., J.-P.E., T.T. and B.A.G. wrote the paper.

**Competing interests** The authors declare no competing interests.

### Additional information

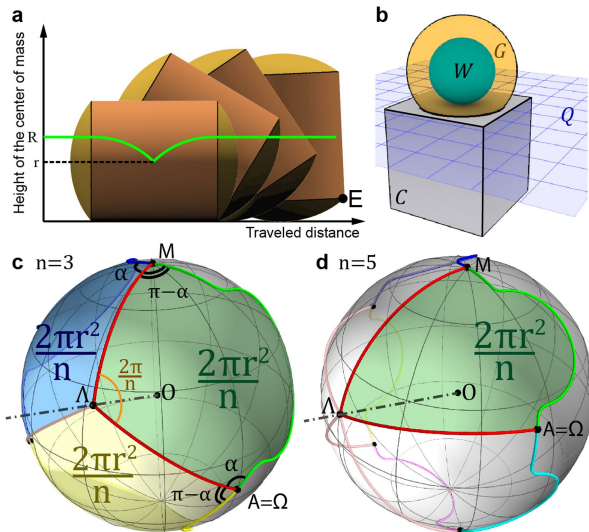
**Supplementary information** The online version contains supplementary material available at <https://doi.org/10.1038/s41586-023-06306-y>.

**Correspondence and requests for materials** should be addressed to Yaroslav I. Sobolev, Tsvi Tlusty, Jean-Pierre Eckmann, Steve Granick or Bartosz A. Grzybowski.

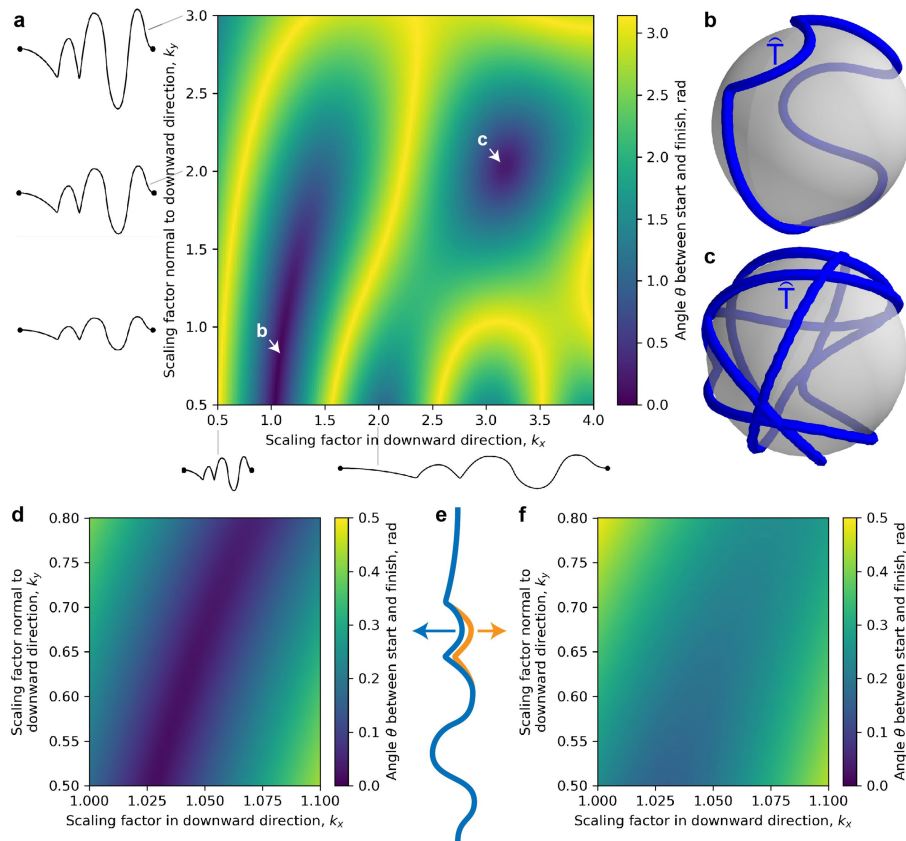
**Peer review information** *Nature* thanks Peter Varkonyi and the other, anonymous, reviewer(s) for their contribution to the peer review of this work.

**Reprints and permissions information** is available at <http://www.nature.com/reprints>.



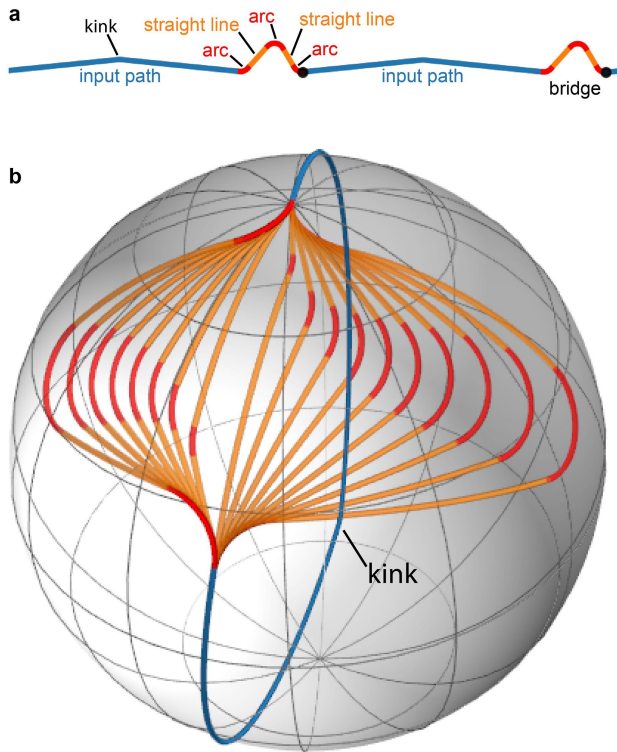


**Extended Data Fig. 1 | Additional illustrations.** **a**, Potential energy curve corresponding to one half of a period of a sideways rolling of a capped-cylinder trajectoid (orange, yellow) from Fig. 1d. The potential energy curve (green) starts at a minimum energy  $mgr$ , follows a cycloid until reaching maximum energy  $mgR$  and remains constant afterwards until the edge  $E$  contacts the plane. In other words, spherical side caps of radius  $R$  define the maximum of the potential surface. Increasing  $R$  increases the  $mg(R - r)$  difference and deepens the “trench” in the gravitational potential surface, making the adherence to the target path  $T_s$  more reliable. **b**, Relative positions of objects defined in the numerical implementation of the algorithm. See Methods for details. Sphere  $G$  (the initial “shell” mesh, radius  $R$ ) is concentric with  $r$ -radius core  $W$  and intersects with the cube  $C$ , whose top face is tangent to  $W$  and lies in the plane  $Q$  of rolling. **c,d**, Illustration of the MPT Theorem (see Methods for details) with the same path as in Fig. 3d for  $n = 3$  (**c**) and  $n = 5$  (**d**).



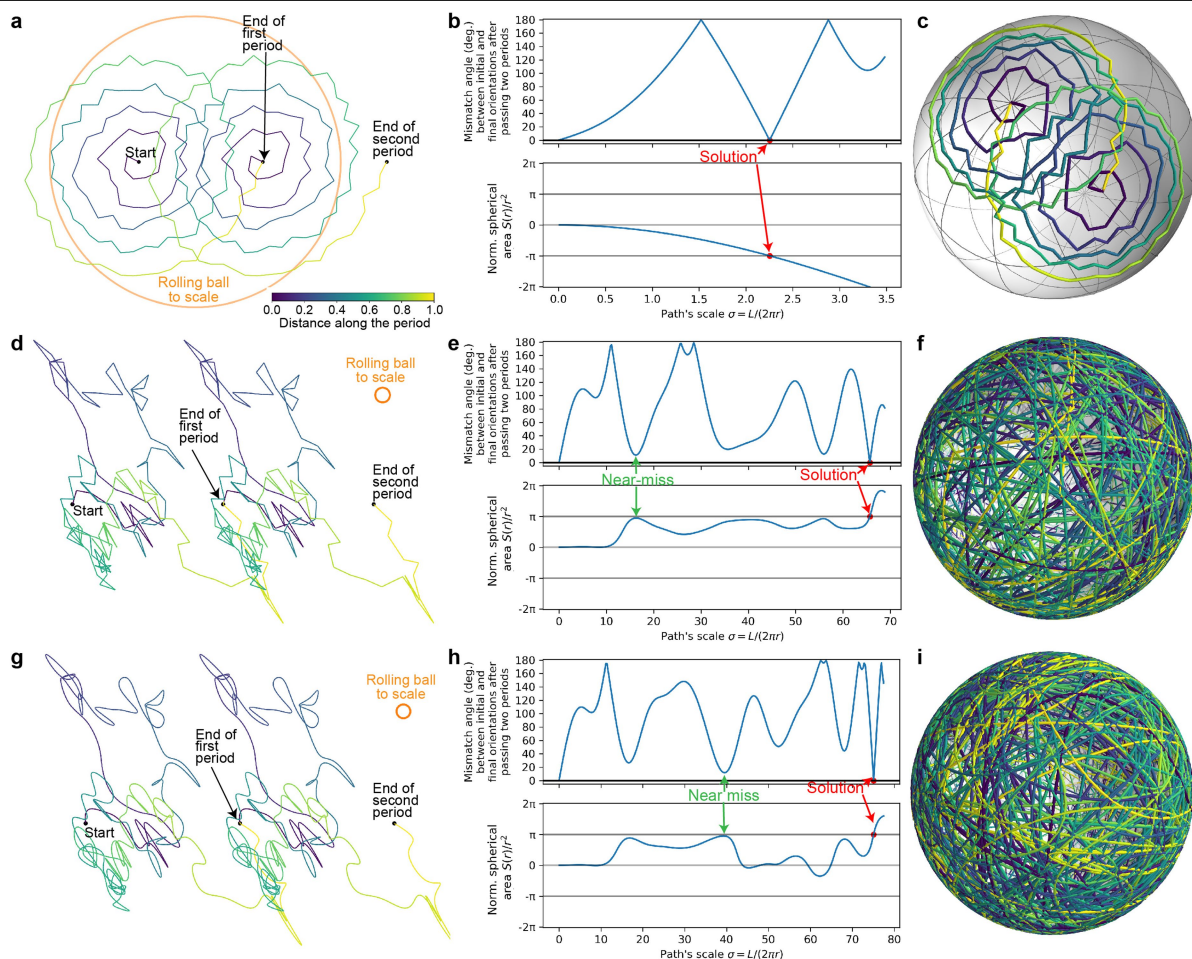
**Extended Data Fig. 2 | Deforming the input path non-uniformly to make it have a one-period trajectoid.** **a**, Angle  $\theta$  between starting and final orientations of a sphere rolled along a target path (same as in Fig. 2a and Fig. 4d) that was deformed non-uniformly in two directions by scaling factors  $k_x$  and  $k_y$  (see Methods for details). Examples of deformed path on the left correspond to  $k_y = 1, 2, 3$  and fixed  $k_x = 1$ ; examples below correspond to  $k_x = 0.5, 2$ , and  $k_y = 1$ . Fulfilling the  $R_{A\Omega} = 1$  condition requires that  $\theta$  be zero (*blue* regions). **b, c**, Curves traced over the sphere by sphere-plane contact point when using paths

corresponding to the local minima marked as b and c in the  $\theta(k_x, k_y)$  map in panel (a). **d-f**, Deformations additional to non-uniform scaling affect the minimal mismatch on the  $\theta(k_x, k_y)$  map: a path (*blue*, same as in Fig. 2a and Fig. 4d) is partially modified by adjusting its Bezier curve nodes; the modified section is shown in *orange* in **e**. Maps (**d, f**) of mismatch angle  $\theta$  for both the original path (**d**) and its modified version (**f**) are plotted for the vicinity of the useful minimum of the original path (see full map in panel **a**). Note the increase of mismatch in **f** compared to **d**.



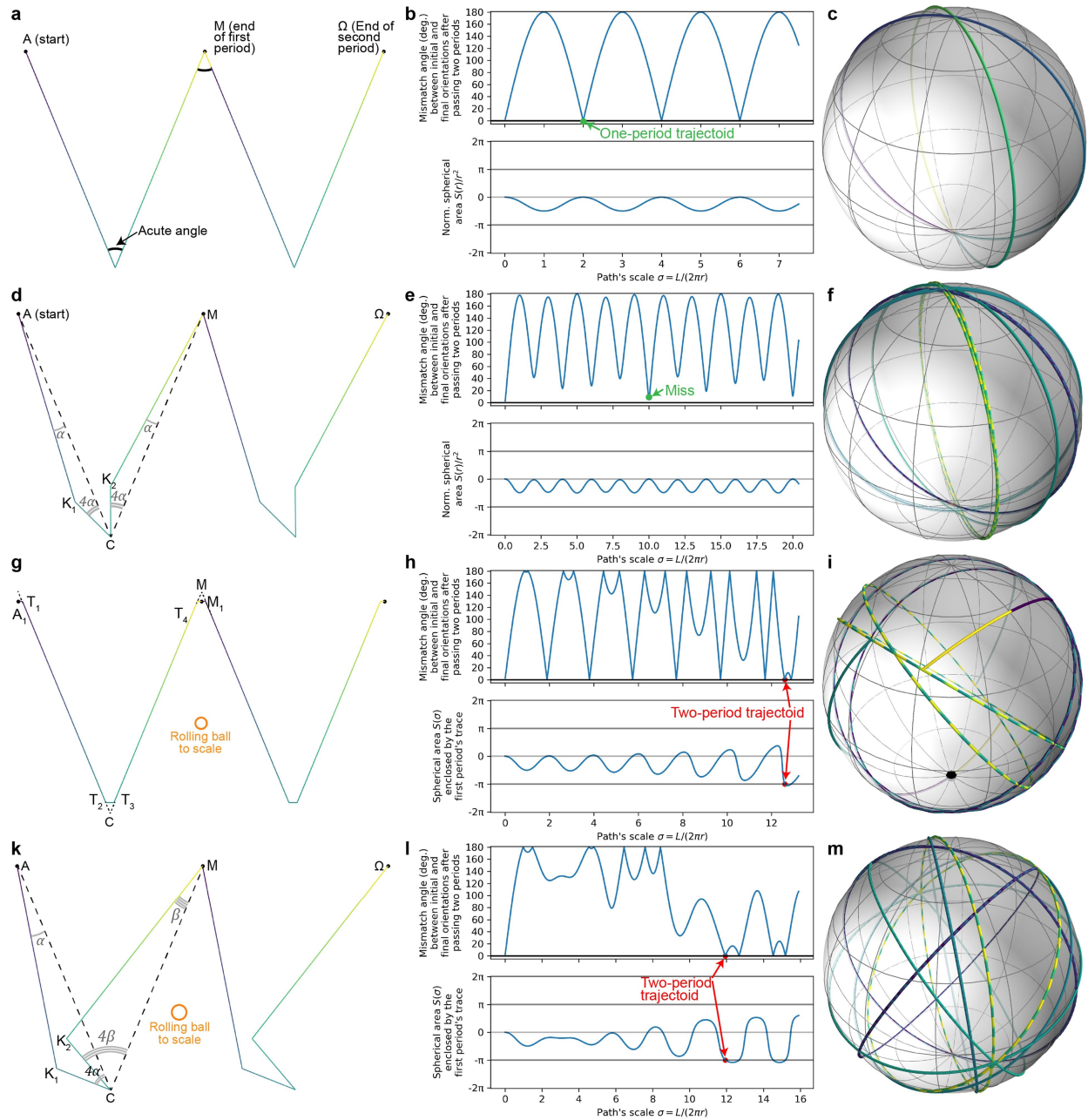
**Extended Data Fig. 3 | “Bridging” the input path to make it have a period-one trajectoid.** Example of input path (*blue*) with “bridges” (*red* and *orange*) appended to it. Bridge consists of three arcs (*red*) and two straight “arms” (*orange*). **b**, Family of bridges constructed for the path in **a** at a fixed scale.





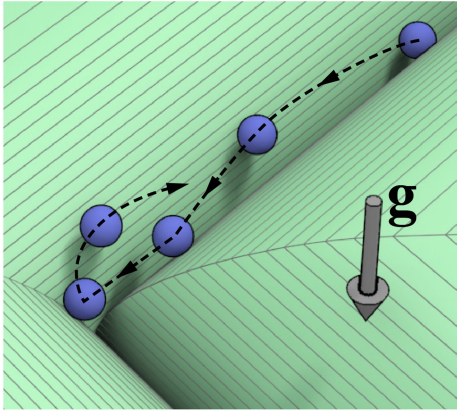
**Extended Data Fig. 4 | Existence of trajectoids completing two periods in one revolution: paths having Property  $\pi$ .** **a,d,g.** Two periods of the input planar, complex paths. Color represents progression within a single period (from blue to yellow, see color scale in a). Orange circle shows diameter of the sphere from **c,f,i** relative to the path. **b,e,h.** Correspond to paths in **a,d,g** respectively. Top plot is the mismatch angle (degrees) between initial and final orientations of the sphere after completing two periods of the scaled path – plotted against the path scale  $\sigma$ . This angle is obtained by Euler’s axis-angle representation of the matrix of net rotation accumulated by the sphere

formula (6) in Methods:  $\theta = \arccos((\text{tr}R_{A\Omega} - 1)/2)$ . Bottom plot in each panel shows oriented spherical area  $S(\sigma)$  enclosed by the spherical trace of scaled first period, also plotted against the scale  $\sigma$ . Scale corresponding to a two-period trajectoid is marked by red dots in respective plots **b,e,h**. **a.** Archimedes spiral with random noise added. **d,g.** Path obtained by a 2D random walk (making equal steps in random directions) – in piecewise linear version (**d**) and smoothed version (**g**).

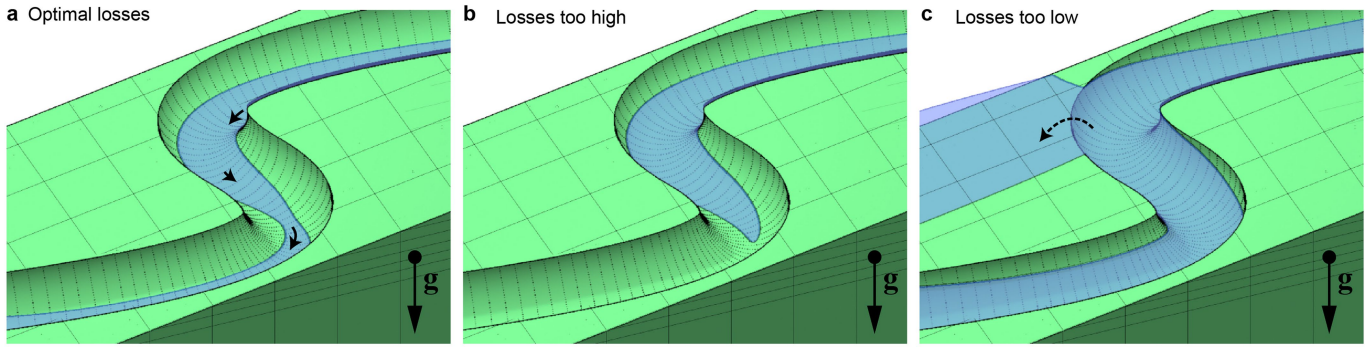


**Extended Data Fig. 5 | Search for paths not having Property  $\pi$ .** Representation analogous to Extended Data Fig. 4, but for different input paths. **a**, Acute-angle isosceles V-path does not have Property  $\pi$ : for this path,  $|S(\sigma)| < \pi$  for all  $\sigma$ . The trace **c** corresponds to a one-period trajectoid as shown by the green dot in **b**. **d**, V-like path whose arms have “kinks” parameterized by angle  $\alpha$ . It does not have Property  $\pi$ , and a two-period trajectoid does not exist for this path. The trace **f** corresponds to a green dot in **e** showing a near miss (i.e., not a trajectoid).

**g**, V-like path similar to the one in panel **a**, but here the acute corners are tapered (“dulled”) by straight segments  $A_1T_1, T_2T_3, T_4M_1$ . Trajectoid for this path exists (red points in **h**). **k**, Asymmetric V-like path with kinks – as in panel **d**, but here kinks in two arms are unequal: angle of the left kink is  $\alpha$ , but angle of right kink is  $\beta = \alpha(1 + \Xi)$ . Trajectoid for this path exists (red points in **l**). In panels **k, l, m**, we used asymmetry  $\Xi = 0.37$ . See Supplementary Video 4 for dependence of these plots on angle  $\alpha$  in **d**, taper ratio in **g**, and asymmetry  $\Xi$  in **k**.



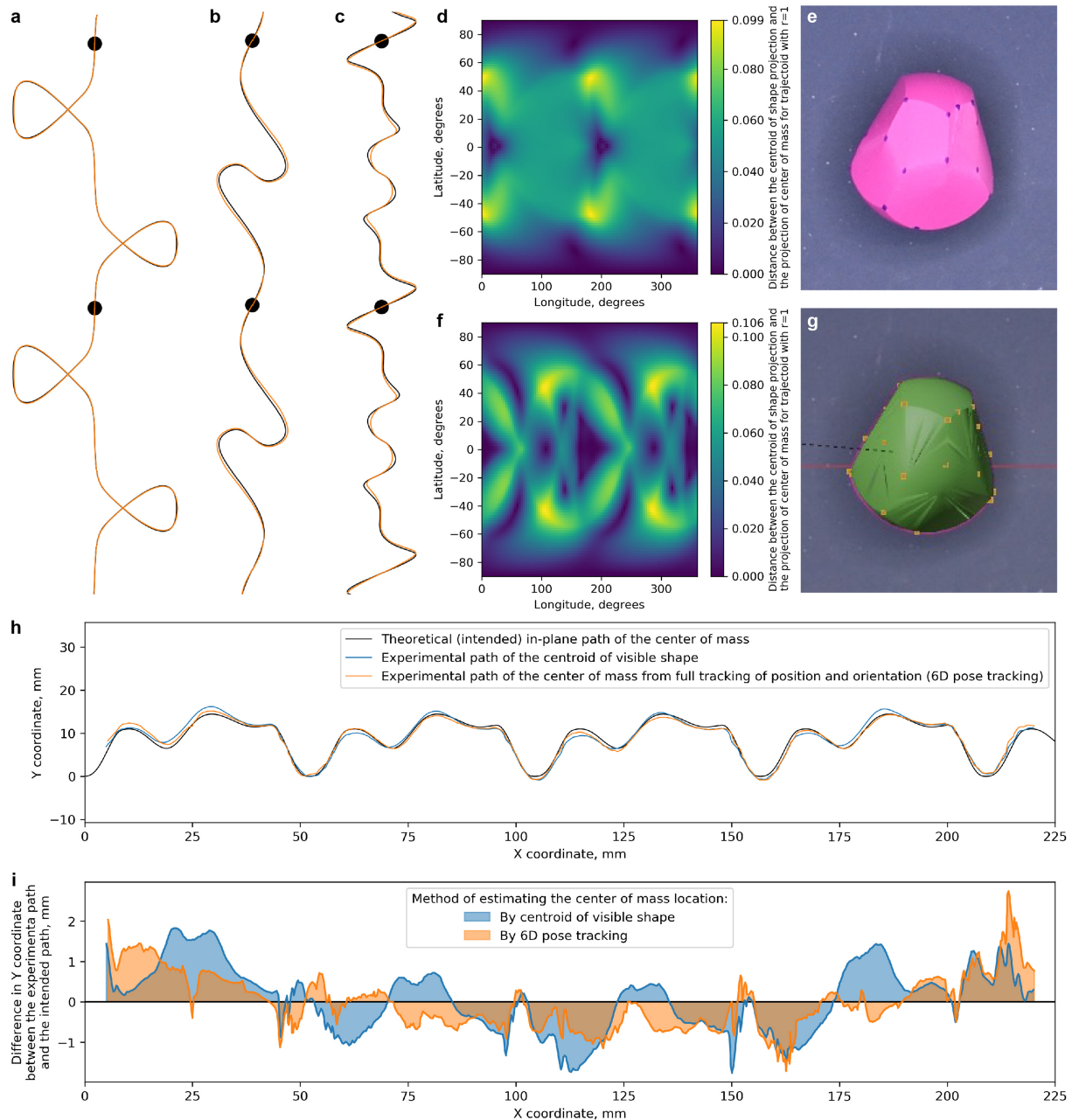
**Extended Data Fig. 6 | Trajectoid tumbling at sharp turns.** In Fig. 4d, g, h, the trajectories feature some sharp turns (marked therein by *green* circles) at which trajectoids tumbled/recoiled. These features of dynamics can be understood by looking at the trench made by the trajectoid in the gravitational potential surface. The representation here resembles Fig. 1b except that the trench makes a sharp turn. In this dynamic analogy, resulting motion can be illustrated by a small particle (colored here in *blue*) rolling down such a trench: prior to encountering a sharp turn, the particle may have a zig-zag trajectory bouncing between the trench walls (cf. Fig. 4d, h yellow arrows), and then might recoil back at the sharp turn instead of making the turn immediately. It may take a few bounces before the particle finally turns the corner. For the actual trajectoids we fabricated, these bounces and zig-zagging correspond to precessions that may result in net rotation of the object around the axis normal to the sloped plane. In the case of the second corner in Fig. 4d (bottom *orange* circle), the unintended net rotation due to recoils causes a turn of the entire subsequent trajectory with respect to the intended path T. We believe that these dynamic defects may be minimized by engineering the trench profile (presently we keep it cycloid-like, which might be overly sharp) or making smoother turns of path T.



**Extended Data Fig. 7 | Energetic considerations for intermittent uphill rolling.** Energy landscapes illustrating design considerations for traversal of uphill excursions (as in the path in the main-text Fig. 4n, o). The gravitational acceleration vector  $g$  (vertical arrow) points down. The trajectoid's total energy (blue surface) decreases with descent due to losses such as friction. The potential energy surface (green) is defined by trajectoid's shape and the angle of the slope. Parts of the potential surface that are below the total energy surface are accessible to the rolling trajectoid. Proper balance between losses, shape, and slope are shown in a: the total energy suffices to overcome the potential barrier along the target path (uphill excursion, short arrows), yet is

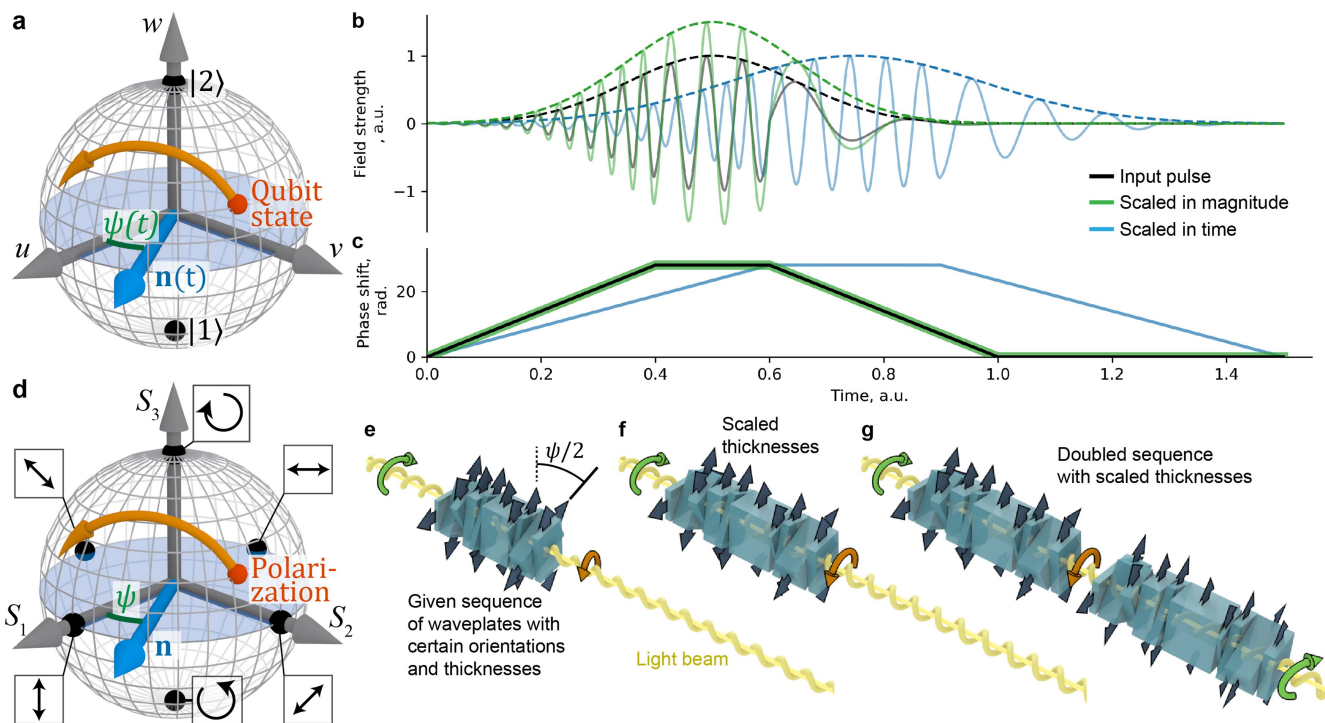
insufficient to escape walls of the potential trench that follow the target path. **b**, When losses are too high, the net energy is insufficient for an uphill excursion. When losses are too low, as in **c**, net energy decreases more slowly than the potential energy and becomes sufficient to escape the potential trench as indicated by the dashed arrow. Note that strictly speaking, the net energy is not a function of only the 2D location on the plane and, furthermore, the potential energy depends on the trajectoid's 3D orientation, which is not an unambiguous function of the 2D planar location even for slipless rolling. Still, the concept of potential landscape is useful as a first approximation.





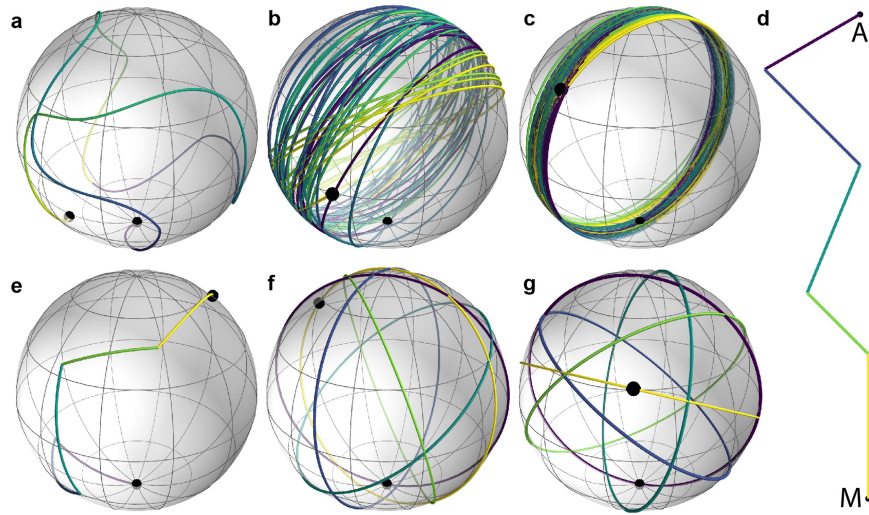
**Extended Data Fig. 8 | Centroid of a visible shape as an estimator of the center of mass. a-c,** Comparisons between the target path of a trajectoid (solid *black* curves) and the theoretical trace of the centroid of trajectoid's shape projection, simulated assuming perfect performance (*orange* curves). The difference between curves in **a** is barely visible. Note that the discrepancy between orange and black curves in **a, b, c** is smaller than or comparable to the discrepancies between the experimental trajectories and the respective target paths (Fig. 4o, n, l). **d, f,** For every possible orientation of the trajectoid (parameterized by latitude and longitude of contact point on the trajectoid), color on these maps shows planar distance between the projection of the center of mass and the centroid of the shape projection. Maps in **d** and **f** are computed for the trajectoids constructed for paths **b** and **c**, respectively. Note that the distance in these maps never exceeds of the trajectoid's minimal radius  $r = 1$ . **e, g,** Illustration of 6D pose (full orientation and position) tracking from video frames (see Supplementary Video 7): **e** is the raw video frame of the

trajectoid (same as in Fig. 4k) whose surface has *black* dots (markers) painted on it; **g** shows the same raw frame overlaid with the trajectoid's green 3D mesh (the one used for 3D-printing the trajectoid) matching the location and orientation evaluated by 6D pose tracking algorithm applied to apparent trajectories of black markers on the video (reconstructed 3D locations of markers are shown in *orange*). **h,** Comparison of theoretical (intended) path of the 2D projection of the center of mass (*black* curve) and the experimental path evaluated by two methods: by the centroid of the visible shape (*blue* curve) or by the 6D pose tracking algorithm (*orange* curve). Both methods were applied to the same video. **i,** Difference in the Y coordinate between the experimental and the intended path for the two methods of evaluating the center-of-mass location: here, the *black* curve in **h** has been subtracted from the *blue* and *orange* curves in **h**, respectively. The standard deviations for the two methods are: 0.845 mm when using centroid of visible shape, 0.765 mm when using the 6D pose tracking.



**Extended Data Fig. 9 | Optical and quantum-mechanical analogies to the existence of two-period trajetoids.** **a**, Illustration of the Bloch sphere representation of a single qubit. The state represented by a red circle on the sphere rotates (orange arrow) around an instantaneous axis  $\mathbf{n}(t)$ , which is defined by the driving field. **b,c**, Field pulse equivalent to a single period  $T$  (**b**, solid curves), its envelope (**b** dashed curves) and phase shift (**c**) as functions of time. Shown are two possible analogies to varying the radius  $r$  of the rolling sphere in case of a given field pulse (black): either scaling the applied pulse's magnitude (green) or stretching the pulse's functions (envelope and phase shift) in time (blue). **d**, Illustration of the Poincaré sphere representation of

polarization state of light. Squares show polarization states corresponding to respective black points: two circular polarizations at the poles and four linear polarizations at the equatorial plane. **e–g**, Given almost any (i.e. those having Property  $\pi$ ) sequence of waveplates (dark blue in **e**), their thicknesses can be scaled (**f**) by such a factor  $1/r$  that the doubled sequence (**g**) has no net effect on polarization state of light (yellow helices) passing through it. In this example, curved green arrow shows left-handed circular polarization, curved orange arrows show right-handed elliptic (**f**) and right-handed circular (**g**) polarization. See also Supplementary Videos 5, 6.



**Extended Data Fig. 10 | Small-radius (“adiabatic”) limit of trajectoids.**  
**a–c,** Effect of ball radius  $r$  (or path’s scale  $\sigma = L/(2\pi r)$ ) on the trace of the contact point upon rolling along a finite smooth path (two periods of path from Fig. 4k). Value of  $r$  decreases from **a** to **b** to **c**. See Supplementary Video 8 for more

details. **d,e–g,** Effect of ball radius  $r$  (or path’s scale  $\sigma = L/(2\pi r)$ ) on the trace of the contact point upon rolling along a polygonal path (path shown in **d**). Value of  $r$  decreases from **e** to **f** to **g**. See Supplementary Video 8 for more details.